

Snakeskin-inspired Elastomers with Extremely Low Coefficient of Friction under Dry Conditions

Mengyuan Wang,^{1,2} Sujan K. Ghosh,³ Christopher M. Stafford,⁴ Adrienne K. Blevins,^{1,2} Sijia Huang,⁵ Jaylene Martinez,² Rong Long,² Christopher N. Bowman,^{1,5} Jason P. Killgore,⁶ Min Zou³ and Yifu Ding^{1,2,}*

¹Materials Science and Engineering Program, University of Colorado, Boulder, CO, 80303, the United States

²Department of Mechanical Engineering, University of Colorado, Boulder, CO, 80309, the United States

³Department of Mechanical Engineering, University of Arkansas, Fayetteville, AR 72701, the United States

⁴Materials Science and Engineering Division, National Institute of Standards and Technology, Gaithersburg, MD, 20899, the United States

⁵Department of Chemical and Biochemical Engineering, University of Colorado, Boulder, CO, 80309, the United States

⁶Applied Chemicals and Materials Division, National Institute of Standards and Technology, Boulder, CO 80305, the United States

KEYWORDS

Coefficient of friction, elastomer, friction reduction, snakeskin inspiration, surface modification.

ABSTRACT

Soft elastomers are critical to a broad range of existing and emerging technologies. One major limitation of soft elastomers is the large friction of coefficient (COF) due to inherently large adhesion and internal loss. In applications where lubrication is not applicable, such as soft robotics, wearable electronics, and biomedical devices, elastomers with inherently low dry COF are required. Inspired by the low COF of snakeskins atop soft bodies, this study reports the development of elastomers with low dry COF by growing a hybrid skin layer with a strong interface with a large stiffness gradient. Using a solid-liquid interfacial polymerization (SLIP) process, hybrid skin layers are imparted onto elastomers, which reduces the COF of the elastomers from 1.6 to 0.1, without sacrificing the bulk compliance and ductility of elastomer. Compared with existing surface-modification methods, the SLIP process offers spatial control and ability to modify flat, pre-patterned, curved, and inner surfaces, which is essential to engineer multifunctional skin layers for emerging applications.

Introduction

Tribocontact-related friction and wear contribute to around 23 % of energy consumption globally, thus efforts to reduce friction have a tremendous impact.¹ In most cases, this is achieved by lubrication using liquids (e.g., oil or water),² solids (e.g., graphite),^{3,4} or sacrificial wear layers typically made of polymers.⁵ Lubrication, however, is often not applicable due to the constraints of working environment or concerns of contamination. Reducing dry friction is particularly challenging for soft materials such as elastomers, which are key components in emerging applications of soft robotics,^{6,7} flexible electronics,⁸ and biomedical devices.⁹ Compared with hard materials (stiffness > 1 GPa), unmodified elastomers (stiffness \approx few MPa) display an order of magnitude higher coefficient of friction (COF) due to both strong interfacial

adhesion and internal loss associated with chain relaxations.¹⁰ Strategies to reduce the COF of elastomers under dry conditions must not sacrifice their inherent flexibility and ductility, which presents a significant materials design/modification challenge.

Nature has provided excellent examples of surface modification strategies to overcome various type of challenge, for example, in wettability,^{11, 12} adhesion (both dry and under water),^{13, 14} antifouling,^{15, 16} and drag reduction.^{17, 18} Herein, we aim to develop elastomers with low COF, inspired by skins of squamate reptiles, especially snakes, which display low COF during fast locomotion without mucus secretion from the skins.¹⁵ The anatomy of the snakeskins²⁰ provides a cue: a stiff keratin-based epidermal layer (stiffness, E , ranges between $3.2 \text{ GPa} < E < 5.0 \text{ GPa}$)¹⁹ which anchors to compliant dermal stratum ($E \leq 1 \text{ MPa}$)²⁰ through flexible and stretchable collagen fiber organizations ($15 \text{ MPa} < E < 585 \text{ MPa}$).^{22, 23} Such a large gradient of stiffness ($\approx 0.1 \text{ GPa } \mu\text{m}^{-1}$),^{19, 22, 23} coupled with multiscale hierarchical textures (e.g., spines and ridges) on the surface of each scale,^{15, 24} enables the snake to effectively minimize contact adhesion on different terrains,^{20, 21} which results in a COF of 0.11 to 0.20 in sliding forward locomotion.^{25, 26} Such a low COF significantly reduces wear of the skin and protects the animals, even in rough terrain. Most critically, such a design does not sacrifice the flexibility and ductility of the dermal stratum, again, critical for the survival of the animals. It is worth noting that snakes do rely on arrays of scales and variable internal pressure to generate tunable and anisotropic friction for locomotion,²⁷ which itself is another inspiring example for macroscale mechanical design.²⁸ The focus in the present work is to engineer elastomers with “materials” responses that mimic the snakeskin, rather than design “system” response that mimic the snake locomotion.

Mimicking such a skin layer on elastomers is challenging. Current surface modification methods such as UV/ozone,²⁹ chemical grafting,^{30, 31} or vacuum-based thin film deposition (e.g. atomic

layer deposition (ALD), molecular layer deposition or (MLD)³² or chemical vapor deposition (CVD)³³ typically yields a bi-layer structure with a weak interface between layers. Sequential infiltration synthesis (SIS),³⁴ an ALD-based method, can infiltrate ceramic oxides into elastomers but with both low penetration depth ($< 1 \mu\text{m}$) and low infiltrate concentration ($< 15 \%$ by mass). Manufacturing wise, SIS is inherently slow due to the large number of vacuum cycles required to achieve measurable amount of infiltration, which limits its application. Here we report a new and versatile method to grow a stiff hybrid skin on an elastomer with gradient stiffness and surface features that mimic snakeskin. The hybrid skin reduces the COF of the elastomer from 1.6 to as low as 0.1 under dry conditions, while maintaining the overall flexibility and ductility of the elastomer.

Results and discussion

Design of the SLIP method on elastomer surfaces

Figure 1 illustrates this simple yet robust process based on a solid-liquid interfacial polymerization (SLIP) process: an aqueous precursor solution (2-hydroxyethyl methacrylate, HEMA, crosslinker polyethyleneglycol dimethacrylate, PEGDMA, and photoinitiator, dimethoxy-2-phenylacetophenone, DMPA) is sandwiched between an elastomer (polydimethylsiloxane, PDMS) and a glass slide, and subsequently photopolymerized into a hydrogel film, during which the growing poly (2-hydroxyethyl methacrylate) (PHEMA) chains infiltrate into PDMS to form a hybrid skin layer. The selection of the PDMS/HEMA system for the SLIP process is based on mechanical, chemical, and thermodynamic considerations. Mechanically, PDMS possesses subcutaneous-stratum-like stiffness ($60 \text{ kPa} < E < 3 \text{ MPa}$, depending on the crosslinking density),³⁵ while PHEMA is glassy at room temperature ($T_g \approx 85 \text{ }^\circ\text{C}$) with stiffness ($\approx 2 \text{ GPa}$)³⁶ comparable with the keratin scale layer. Chemically,

HEMA/siloxane-based formulations have been commercialized in soft contact lenses, in which the optimized ratio of hydrogel and siloxane ensures the biocompatibility and excellent moisture and oxygen permeability.³⁷ Thermodynamically, HEMA/PDMS system is effective for infiltration using the SLIP process. PDMS (solubility parameter, $\delta_{\text{PDMS}} = 7.3 \text{ cal}^{1/2} \text{ cm}^{-3/2}$)³⁸ is incompatible with HEMA ($\delta_{\text{HEMA}} = 13.1 \text{ cal}^{1/2} \text{ cm}^{-3/2}$).³⁹ The swelling of PDMS by pure HEMA (a liquid at room temperature) is non-detectable, and the subsequent photopolymerization results in no surface modification on PDMS (**Figure S1**). However, the compatibility changes in the presence of water ($\delta_{\text{H}_2\text{O}} = 23.4 \text{ cal}^{1/2} \text{ cm}^{-3/2}$), which is a nonsolvent for PDMS, but a good solvent for HEMA (isomorphous at room temperature). Control experiments revealed a mass increase of 0.64 mg for a PDMS film (area = 1.21 cm², thickness \approx 450 μm , total mass 50 mg) after being immersed in an aqueous HEMA precursor solution (20 % by mass) for 15 min. Upon photopolymerization using the same precursor solution, the mass uptake Δm_s (subscript *s*, swelling state) for the PDMS increased to 4.34 mg and then decreased slightly to $\Delta m_d = 3.27$ mg after drying for 12h under a chemical hood (subscript *d*, dry state). This result suggests that water accounts for 26 % ($= (\Delta m_s - \Delta m_d) / \Delta m_s$) of the total mass uptake by the PDMS during the SLIP process. Collectively, these measurements confirm that the photopolymerization of an aqueous HEMA precursor solution in contact with a PDMS film results in significantly more PHEMA infiltration into the originally immiscible PDMS.

The mechanism for enhanced infiltration is associated with the reduction in miscibility between water and PHEMA during the polymerization/crosslinking, which is commonly attributed to both the reduction in Flory-Huggins mixing entropy and the increase in elasticity of the crosslinking PHEMA network.⁴⁰ For example, the maximum swelling ratio of water in bulk polymerized HEMA/PEGDMA film is only 38 % by mass (of the total hydrogel),⁴¹ as confirmed by our

experiments. For a HEMA precursor solution containing more than 38 % by mass water, photopolymerization will result in phase separation between the PHEMA network and water. This change in thermodynamic mixing energy drives more PHEMA chains, together with a certain amount of water, into the contacting PDMS, as illustrated in **Figure S2**.

Based on the above analyses, we investigated the SLIP process using three precursor solutions with HEMA to water concentrations of 20 %, 40 %, and 60 % by mass, and the modified PDMS samples are referred to as HEMA_20, HEMA_40, and HEMA_60, correspondingly. PDMS samples with a precursor: crosslinker ratios of 5:1, 10:1 and 20:1 were investigated. Besides flat surfaces, PDMS with surface patterns fabricated by soft lithography (**Figure S3**) and microchannels were modified. Unless specified, all the samples were processed with 15 min pre-soaking time, 15 min photopolymerization under 365 nm (20 mW cm^{-2}) UV irradiation, and “PDMS” refers to 10:1 curing ratio (otherwise, PDMS 5:1 and PDMS 20:1). A detailed protocol is provided in the Materials and Methods section and all the formulations reported are listed in **Table S1**.

Snakeskin-inspired structure and low surface friction behaviors

Figure 2a shows an example of a PDMS film that has an outlined region with a skin layer grown using the SLIP process with HEMA_20. The unmodified regions of the PDMS remain transparent and highly adhesive, as demonstrated by the strong adherence of a 5 g mass standard even at a 90° inclination. Upon surface modification using the SLIP process, the skin layer reduces the normal light transmittance of the PDMS from $\approx 92.9 \%$ to 10.5% , which transforms the PDMS to opaque (optical measurement details are provided in **Materials and Methods and Supporting Information**). The significant scattering of light is caused by the randomly oriented creases across the skin layer (**Figure 2b**), which are due to the compressive loading by bulk

PDMS on the swollen skin layer.^{42,43} From profilometer measurement across the boundary (**Figure 2c**), the modified region is $\approx 17 \mu\text{m}$ thicker than the unmodified region. A cross-sectional image of one of the creases (**Figure 2d**) reveals that the fractured skin layer appears more textured and rougher than the bulk PDMS that is smooth due to brittle failure. Based on such a fractographic contrast, the skin layer is highlighted by the false-colored SEM image in **Figure 2d**, which is corresponding with the color shown in anatomy of snakeskin.²⁰

The SLIP method is versatile, as highlighted in **Figure 2e** and **2f**. Because infiltration is facilitated by photopolymerization, the method allows growth of the skin layer in a spatially controlled fashion. As demonstrated in **Figure 2e**, the skin layers grow on UV irradiated regions through a customized photomask, forming the “SLIP” acronym. Like other mask-based, diffusion-limited patterning techniques, we expect the spatial resolution of the SLIP process to be between $5 \mu\text{m}$ and $10 \mu\text{m}$. In addition to non-patterned or pre-patterned PDMS films, SLIP can modify curved surfaces, provided good contact between a precursor solution with the elastomer. As demonstrated in **Figure 2f**, a skin layer grows on the inside lumen of a PDMS microchannel, simply by photopolymerization of the HEMA precursor solution after filling the channel. In comparison, it is challenging to selectively modify such inner walls by existing surface treatment methods based on molecular depositions or doping.

We first compared virgin PDMS with HEMA_20 (the sample shown in **Figure 2a**) using a static sliding friction test with a deadweight and a slope (**Figure S4** and **Movie S1**). The static friction coefficient is calculated from, $\mu_s = h/l$, where h and l are the height and length of the slope when the weight (20 g) starts to slide. For virgin PDMS, the adhesion is strong enough to prevent any sliding at any inclination angle, even at 180° (upside down). In stark contrast, the HEMA_20 displays an exceptionally low value of COF, $\mu_s = 0.14 \pm 0.04$, which matches that of snakeskin in

forward locomotion.^{25, 26} This comparison clearly demonstrates that the skin layer formed effectively reduces the adhesion contribution to the COF, imparting a slippery surface on the elastomer without lubrication. This is consistent with prior studies showing that PDMS surface wrinkles from oxygen plasma treatment displayed lower adhesion strength than flat PDMS surface.^{44,45} Given that the static sliding test is incapable of testing virgin PDMS, a ball sliding friction test with varying load was carried out for all the samples prepared, as discussed later.

Surface morphologies and chemical analysis of the SLIP modified elastomer

A benefit of the SLIP process for skin layer growth is that the skin layer is robust and tunable by process parameters. **Figure 3a – 3c** present examples of the skin layer grown on flat PDMS with the three HEMA precursor solutions, displaying characteristic swelling-induced crease morphology. From the mass measurements discussed earlier, the SLIP with a HEMA₂₀ precursor solution on a 450 μm thick PDMS (50 mg) leads to 4.34 mg PHEMA uptake, i.e. an 8 % mass increase. Correspondingly, the effective PHEMA concentration within the PDMS surface layer would be 80 % (or 56 %) for an infiltration depth of 10 μm (or 30 μm). Such a significant surface swelling is constrained by the unswollen bulk PDMS, which results in the crease instability.^{41,42}

Crease formation is commonly observed during constrained swelling or drying in hydrogels⁴⁶ and block copolymer films.⁴⁷ Increasing water content in the HEMA precursor solution causes the creases to evolve from isolated (Figure 3a) to cuneiform-like morphology (Figure 3b and 3c) with increasing aspect ratio.⁴⁷ From an instability analysis, this trend in morphology reflects higher compressive strain and/or larger skin layer stiffness,⁴⁸ both of which are related to the HEMA mass uptake in the skin layer. The isolated creases, reflecting lower degree of swelling and lower modulus gradient in the skin layer, are similarly observed during swelling of a piece of

dry hydrogel.^{42, 49} From stylus measurements (as summarized in **Table S2**), the wavelengths of the crease are comparable with the upper range of ventral scales of snakes (5 μm to 30 μm),⁵⁰ while the amplitudes of the crease are larger. Cross-sectional SEM images of the skin layers (**Figure 3d – 3f**) reveal a similar trend: thicker skin layers, as approximated by the roughness of the fractured surface, for samples modified with higher-water-content precursor solutions.

Supporting Information illustrates the summary of the SLIP parameters studies. Increasing UV exposure from 15 min to 30 min does not impact the skin layer morphology but induces secondary creases perpendicular to primary creases (**Figure S5a**). Such fine and hierarchical structure formation is attributed to release and localization of the elastic energy during the crease formation.⁵¹ The wavelength (λ) of the creases formed on PDMS with varying crosslinking density (modulus, E_s) can be rationalized by the classical buckling relationship: $\lambda \propto E_s^{-1/3}$.⁵² PDMS 5:1 displays similar skin layer morphology as PDMS 10:1 (**Figure S5b**) because they have similar moduli.⁵³ In contrast, PDMS 20:1 shows larger feature sizes (**Figure S5c**) with the aspect ratio reaching 0.41 without forming cracks (**Table S2**), which is consistent with its low modulus (60 kPa).

To better understand the surface modification, the chemical composition and stiffness of the skin layers grown under the above-mentioned conditions were characterized. Both Attenuated Total Reflectance Fourier Transform Infrared (ATR-FTIR, probing depth 1 μm to 2 μm , **Figure S6** and **Table S3**) and X-ray Photoelectron Spectroscopy (XPS, probing depth 5 nm to 10 nm, **Table S4**) measurements confirmed that the skin layers are composed of both PHEMA and PDMS. Assuming the PHEMA/PDMS composition within the XPS sampling depth is constant, the measured atomic percentage, and accordingly the estimated mass and volume fractions (see **Supporting Information** for detailed conversion), of the PHEMA within the top of the skin

layers are shown in **Figure 3g**.⁵⁴ The data confirm that an increase of water mass fraction in the precursor solution from 40 %, to 60 %, to 80 % leads to an increase of PHEMA infiltration from 11.3 %, to 46.4 %, and to 69.2 %, in agreement with the infiltration mechanism discussed earlier. Correspondingly, such an increase in PHEMA content makes the skin layer more hydrophilic, with water contact angle (WCA, **Figure 3h**) decreasing from 111.7°, to 64.0°, to 53.4°, respectively. For reference, pure PDMS and PHEMA display WCA of 107.8°⁵⁵ and 37.9°,⁵⁶ respectively. The slight increase in WCA for the skin layer containing 11.3 % PHEMA is attributed to an increase in the surface roughness (**Figure 3a – 3c**).⁵⁷

Surface and bulk mechanical characterization of the SLIP modified elastomer

Based on the percentage of PHEMA, the surface modulus of the skin layers, E_s , can be estimated using a mixture rule,⁵⁸

$$E_s = \Phi_P E_P + \Phi_H E_H \quad (1)$$

Where Φ_P and Φ_H are the volume fraction of PDMS and PHEMA, while E_P and E_H are the Young's modulus of PDMS (1.74 MPa \pm 0.15 MPa) and PHEMA with 5 % cross-linker (2.53 GPa \pm 0.22 GPa) as measured by dynamic mechanical analysis (DMA) (**Table S5**).³⁶ The calculated modulus of the hybrid skin layers ranges from 0.24 GPa to 1.65 GPa, which is up to 3 orders of magnitude stiffer than the bulk PDMS, and comparable with the keratin layer of the snakeskin.

Additionally, we directly measured the modulus of the skin layers using atomic force microscopy (AFM) fast force mapping.^{26, 59} The average values obtained for each sample are plotted in **Figure 4a**, and the corresponding modulus maps for HEMA_60 and HEMA_20 are shown in **Figure 4b** and **4c**). The experimental values display the same trend as the values calculated from

the rule of mixture, but absolute values are slightly lower. This discrepancy could be attributed to the fact that the indentation-based AFM measurements probes a larger depth than the XPS, reaching regions with lower PHEMA concentrations (and correspondingly lower stiffness). Furthermore, AFM measurements also show a skin layers on the PDMS 20:1 that is stiffer ($E = 1.87$ GPa, **Figure S7**) than on PDMS 10:1 prepared under identical SLIP conditions ($E = 1.57$ GPa, **Figure 4c**), suggesting a higher degree of PHEMA infiltration consistent with the larger creasing structures observed (**Figure S5**). The high-resolution modulus maps also reveal that the skin layer is microscopically heterogenous for HEMA_60 (**Figure 4b**) with stiff, PHEMA-rich domains (size $55.9 \text{ nm} \pm 19.4 \text{ nm}$) dispersed within the soft PDMS-rich continuous phase. A phase inversion occurs with an increase of the PHEMA concentration (**Figure 4c and Figure S7**), as the stiff PHEMA phase becomes the continuous phase.

To determine the impact of the skin layer formation on the overall mechanical characteristics of the PDMS, we measured stress-strain responses (**Figure 4d**) of all the samples under uniaxial tensile loading. The Young's modulus, ultimate tensile strength, and failure strain from the measurements are summarized in **Figure 4e**. The PHEMA infiltration in the skin layer only slightly increases the overall stiffness of the PDMS, up to 18 % for the sample with the highest PHEMA infiltration (HEMA_20). Perhaps the most significant impact is that the skin layer reduced the engineering failure strain from $102.3 \% \pm 12.1 \%$ to $52.6 \% \pm 8.4 \%$, progressively with the increase of PHEMA content in the skin layers. This naturally leads to a proportional reduction in the ultimate tensile strength. Such a reduction in ductility is expected from both the formation of a continuous glassy layer with creases acting as stress-localization features. Nevertheless, even the lowest failure strain, exhibited by HEMA_20, is well within the range of snakeskins (17 % to 69 %) from different species and habitats.^{22, 23} Furthermore, the reduction in

failure strain, if necessary, is mitigated by designing (or patterning) a discontinuous skin layer, as observed in the arrays of the scales on snakeskin, to minimize the stress localization. In brief summary, the above analysis shows that the SLIP process effectively imparted hybrid HEMA/PDMS skin layers with up to 3 orders of magnitude higher stiffness than bulk PDMS while preserving its overall softness and ductility. Such a snakeskin-like large gradient stiffness associated with diffusional infiltration yields a strong interface that prevents delamination under loading.⁴⁸

Tribological study of the SLIP method modified elastomer surfaces

To quantify the COF for all the samples prepared (including virgin PDMS), we implemented a sliding friction test under automatically controlled 1 N, 5 N, and 10 N normal loads with a velocity of 10 mm/s under a relative humidity of 20 %.⁶⁰ The dynamic COF μ_D during sliding is calculated from,

$$\mu_D = f/P \quad (2)$$

where f is the sliding frictional force under the normal load P . The average COF from 100 cycles (**Figure S8**) of measurements under 1 N normal force for virgin and modified PDMS samples are shown in **Figure 5a**. For virgin PDMS, the $\mu_D = 1.6$ is a typical large value for elastomers.⁶¹ In stark contrast, the skin layers reduced the COF for all PDMS samples by nearly 10 times ($\mu_D = 0.14$ to $\mu_D = 0.18$), reaching the typical values for snakeskin. As a validation, the value for HEMA_20 obtained from the dynamic sliding test matches well with that obtained from the static friction test mentioned earlier (**Figure S4** and **Movie S1**).

Interestingly, the data indicates that the μ_D of the modified PDMS is nearly independent of the PHEMA percentage for all three modified samples. By approximating the skin layers as smooth

and homogenous layers, the mechanical contact between the chrome-steel sphere and the PDMS films (illustrated in **Figure 5b**) were simulated using Finite Element Modeling (FEM) analysis (**Figure S9**). Under 1 N normal force loading, a smooth stiff skin layer (thickness $\approx 10 \mu\text{m}$) atop the bulk PDMS reduces the apparent contact area ($A_0 \approx \pi a^2$, a is the contact radius shown in **Figure 5b**) from 0.91 mm^2 for unmodified PDMS, to 0.87 mm^2 , 0.78 mm^2 , and 0.76 mm^2 for HEMA_60, HEMA_40, and HEMA_20, respectively (**Table S6**). Correspondingly, the contact (deformation) depth (h_c , **Figure 5b**) reduces from $\approx 0.15 \text{ mm}$, to 0.14 mm , 0.13 mm , and 0.13 mm . This analysis confirms the critical importance of the surface features on these skin layers, which are not captured by the FEM simulations, on the contact deformation of the surfaces. These features could cause more substantial reduction in contact area due to local asperities. A more rigorous mechanical analysis with the knowledge of the stiffness gradient (rather than a homogenous skin layer) is needed to precisely predict the contact deformation. Unfortunately, it has been challenging for us to directly measure the depth-dependent modulus on the cryomicrotomed PDMS skin layer using AFM.

To determine the origin of the COF reduction for the SLIP samples, **Figure 5c** shows the dynamic COF of the PDMS samples as a function of $P^{-1/3}$, where $P = 1 \text{ N}$, 5 N , and 10 N as used in the experiments. For virgin PDMS, a linear correlation between μ_D and $P^{-1/3}$ is observed ($R^2 = 0.98$), which is expected by considering the relationships between normal force, frictional shear stress, and contact area for the smooth PDMS (see **Supporting Information** for the derivation).

⁶² Interestingly, an inverse relationship is observed for all the modified PDMS samples. For HEMA_60 and HEMA_40, μ_D increases only slightly with the increase of load, up to 0.3 and 0.2, respectively, under 10 N (i.e. $P^{-1/3} = 0.46$) loading. In contrast, μ_D of HEMA_20 increases to 0.6 under 10 N loading, which is only slightly below the value of virgin PDMS under the same

loading condition. As derived in the **Supporting Information**, the Coulomb friction behavior (load independent μ_D , as seen for HEMA_60 and HEMA_40) is expected when frictional shear stress (τ) is constant under a given sliding velocity, while an increase of μ_D with P (as seen for HEMA_20) is expected when τ increases with P .

Aside from increasing surface stiffness, contact area and thus COF, can separately be reduced by engineering the surface topography.⁶³ Indeed, we fabricated PDMS patterned with a microlens (diameter $5.1 \pm 0.4 \mu\text{m}$) array using soft lithography with templates fabricated with breath-figure templated self-assembly (**Figure S3**).⁶⁴ Mechanically, the dome-shaped microlens is effective at reducing contact area, which leads to a four-fold reduction in μ_D compared with non-patterned PDMS (from 1.6 to 0.43, **Figure 5a**). With subsequent SLIP modification, the skin-layer (**Figure 5d**) imparts an additional four-fold reduction in μ_D , from 0.43 to 0.12 and 0.1, with HEMA_40 and HEMA_20 precursor solutions. **Figure 5e** shows a skin layer grown on PDMS pre-patterned with Sharklet features (width and height of the lines $\sim 2 \mu\text{m}$).⁶⁵ Similar to the microlens example, the presence of the Sharklet pattern on PDMS alone reduces the μ_D from 1.6 to 0.92, and a further reduction to ≈ 0.2 was achieved with SLIP process. These comparisons show that the combination of stiffness and surface features are important for achieving ultralow COF for elastomers under dry condition, presumably by minimizing contributions from adhesion and/or internal loss from bulk PDMS.

In nature, a great variety of microstructures on the scales of snakes have evolved to adapt to different habitats: leaf-like or ridge-like micro-/nanostructures that offer better camouflage,²⁴ spines with a few-micrometer scale that inhibit wetting and contamination,¹⁵ and net-like micro-ornamentations to further reduce the friction resistance during sliding.²⁶ The integration of SLIP with other fabrication/lithography techniques offers a path to engineer skin layers that capture

the complexity, and thus achieve multifunctionalities, of the different snakeskins. For example, the combination of the SLIP process with Sharklet patterning (**Figure 5e**) not only reduces the COF, but also reduces the normal (i.e. at 0 ° incident angle) light transmission of PDMS to only 2 % while maintaining a total (i.e. at all forward angles) transmission of 88% (Figure S11). Such a light-diffusing capability compares favorably with commercial optical diffusers. Such synergistic benefits of the SLIP with patterning may be in addition to known benefits of the sharklet pattern such as its resistance against microbial attachments.¹⁵

We further confirmed the friction reduction in PDMS 20:1 system (**Figure 5f**), which shows a similar trend as PDMS 10:1. Despite its lower modulus, virgin PDMS 20:1 shows lower μ_D than PDMS 10:1. This phenomenon is attributed to the presence of more free and dangling chains in PDMS 20:1, as this ratio is off-stoichiometry for the formulation, which enhances the lubrication effect.⁶⁶ Upon SLIP modification, μ_D of the PDMS 20:1 reduced to 0.12, 0.18, and 0.14 when HEMA_60, HEMA_40 and HEMA_20 precursor solutions were used, respectively. The applicability of the SLIP on the more compliant elastomer substrate further extends the stiffness ratio between surface and bulk with a low-friction surface and a robust interface, as manifested in snakeskins.

Conclusion

In conclusion, we report controlled growth of hybrid skin layers on elastomers with large stiffness gradient and strong interface inspired by snakeskins. Using a SLIP process, hybrid PHEMA/PDMS skin layers with tunable composition and morphology were demonstrated. Without sacrificing the overall compliance and ductility, the skin layers reduced the COF of PDMS with varying crosslinking density by more than 10-fold, reaching the value observed in snakeskin. The method offers spatial control with photopatterning, compatibility with other

fabrication techniques such as soft-lithography, and the ability to modify curved inner surfaces. With the rapid development of elastomer-based technologies such as soft robotics, the work presented here provides a unique capability to design multifunctional skins with low frictional loss.

Materials and Methods

Precursor solution preparation

The aqueous precursor solution contains HEMA (monomer), poly (ethylene glycol) dimethacrylate (PEGDMA, crosslinker) with $\overline{M}_N = 750$ g/mol, and 2,2-Dimethoxy-2-phenylacetophenone (DMPA, photo initiator). Chemical structures of these components are shown in **Figure 1** of the main text. The homogenous solution was prepared by (1) sonicating HEMA, PEGDMA (5 % of HEMA by mass) and DMPA (1 % of HEMA by mass) mixture; (2) adding different amount of DI water in to above-mentioned mixture to reach water concentration to 40 %, 60 % and 80 % by mass; (3) degassing before casting onto PDMS substrates.

PDMS substrate preparations

PDMS films (Sylgard 184, Dow Corning) with base-to-curing-agent ratio of 5:1, 10:1 and 20:1, were cured at 80 °C for 2 h, and were cut into 30 mm × 30 mm pieces (\approx 5 mm thick) for the subsequent experiments. Surface-patterned PDMS films were prepared using soft lithography. Two surface patterns were fabricated: a microlens array and a Sharklet AFTM features. The microlens patterns with diameter of 5.01 ± 0.37 μ m were replicated from a template fabricated using breath-figure templated assembly,⁶⁴ while the Sharklet pattern with both the width and height of ~ 2 μ m⁶⁵ was replicated from a commercial template from Sharklet Technology (Aurora, CO, USA). Images of the two patterned PDMS samples are shown in **Figure S3**. A

PDMS microchannel was used for demonstrating the SLIP process. The microchannel was cast using PDMS 10:1 mixture into a homemade chamber of two concentric cylinders (inner radius is 0.8 mm and outer radius is 1.4 mm). All the patterned PDMS and PDMS microchannel were cured using the same protocol as the non-patterning films.

SLIP process

As illustrated in the main text (**Figure 1**), a given HEMA precursor solution was drop cast atop a PDMS substrate and capped with a glass slide using a 1 mm thick spacer. After conditioning for 15 min, the sample was irradiated with a UV light (365 nm, 20 mW cm⁻²) for 15 min or 30 min. Next, the slide and the crosslinked PHEMA hydrogel film were removed. The PDMS surface was then rinsed thoroughly with DI water and dried under ambient condition. In this study, the PDMS substrate properties (crosslinking density, no pre-patterning and pre-patterned) and aqueous solution concentrations of HEMA were systematically compared. All the samples examined are listed in **Table S1**.

Bulk PHEMA hydrogels preparation

As control samples, bulk polymerization of all the HEMA precursor solutions (HEMA-water ratios of 20-80, 40-60, and 60-40), as well as HEMA/PEGDMA/DMPA precursor (no solvent), were carried out. All three precursor solutions led to phase-separated hydrogels (indicated by the light scattering). The polymerized bulk PHEMA (a solid film) was swollen in DI water overnight to determine its equilibrium water absorption.

Mass uptake measurement

Mass uptake of the PDMS was measured in three following scenarios using identical PDMS substrates with a thickness of 458 μm and an area of 1.21 cm²: (1) PDMS after being immersed

in pure HEMA monomer (liquid at room temperature) for 15 min; (2) PDMS after being immersed in an aqueous HEMA solution (20 % by mass) for 15 min; and (3) PDMS after the SLIP process using a 20 % by mass HEMA precursor solution. In scenario (1), no mass uptake was measured. In scenario (2), a mass increase of 0.64 mg was measured, indicating small amount of precursor solution infiltrated into the PDMS surface. In scenario (3), the mass increase was $\Delta m_s = 4.34$ mg, suggesting significantly higher amount of mass infiltration. After drying, the mass increase was reduced to $\Delta m_d = 3.27$ mg.

Chemical composition analysis of HEMA/PDMS hybrid skin layer

Attenuated total reflection Fourier Transform infrared (ATR-FTIR) measurements were carried out on a FTIR spectrometer (Nicolet 8700) with attenuated total reflectance (Smart ARK, Thermo Fisher Scientific). Spectra were collected on a ZnSe crystal and were averaged over 32 scans with a resolution 4 cm^{-1} . The angle of incidence on the Smart ARK was set to match the ZnSe crystal (45°). A pressure clamp was used to ensure intimate contact between the sample and the crystal.

X-ray photoelectron spectroscopy (XPS) measurements were performed on a Kratos AXIS Ultra DLD spectrometer with a mono-chromated Al $K\alpha$ source operating at 1486.6 eV and 140 W. The base pressure of the sample analysis chamber was $\approx 2.0 \times 10^{-9}$ Pa, and spectra were collected from a nominal spot size of $300\ \mu\text{m} \times 700\ \mu\text{m}$. Atomic composition was determined from survey scans over a binding energy range of (0 to 1200) eV, pass energy of 160 eV, step size of 0.5 eV, and dwell time of 0.1 s. All XPS data analysis was performed using the CasaXPS software package.

Water contact angle (WCA)

WCA measurements were carried out to determine the wettability of the PDMS surfaces. A sessile-drop method (2 μL DI-water droplet) was used with a custom-built image system (Fastcam SA4, Photron). For each sample, at least three repeated measurements were carried out, and the average values are reported here.

Scanning electron microscopy (SEM)

SEM measurements of both the surface and cross-sectional morphologies of the SLIP-modified PDMS surface were characterized by field-emission SEM (FESEM, JEOL JSM-7401F). The cross-sections were prepared by freeze fracture in liquid nitrogen, and all the samples were coated with a 5 nm platinum layer before the measurement.

Profilometer

Profilometer (Dektak 3030) measurements were carried out to determine the surface profile of the skin layer. A stylus with 12.5 μm radius is equipped with 1 mN force loading on the sample. For each measurement, the stylus scans 30 μm in the horizontal direction at a low speed. The values reported here is the average of 6 measurements from randomly selected regions across the surface.

Atomic Force Microscopy (AFM)

AFM (Cypher, Oxford Instruments) based indentation measurements were carried out to probe the nanoscale mechanical properties of the skin layer, using a fast-force mapping mode. This technique provides a rapid force-volume mapping of surfaces, which calculates a spatially resolved sample modulus. A cantilever with a spring constant of 27.8 N m^{-1} (PPP-NCLR, Nanosensors) was chosen as it provided optimal sensitivity when performing force curves on the samples. An indentation force of 150 nN was chosen for mapping since the resulting indentation

depth, $10 \text{ nm} \pm 2 \text{ nm}$, provided sufficient signal for a contact mechanics model to calculate sample modulus. The default Hertz contact mechanics model was used to fit the force curves, using a tip radius of 15 nm, determined from a calibration measurement on polystyrene ($E = 2.8 \text{ GPa}$), as an input into the model. The z-axis in the resulting images represents the surface topography while the color overlay displays modulus.

Transmission characterization of modified elastomer

UV-vis-NIR spectrophotometer (Cary 5000i, Shimadzu UV-3101PC) was used to measure the transmission of SLIP-modified PDMS (2 mm in thickness with one surface treated), including the normal transmission and the total transmission. The normal transmission was measured with light detector for all light transited within 4° of absolute normal transition. The total transmission was tested on the same UV-vis-NIR spectrophotometer coupled with an integrating sphere (Shimadzu ISR 3100). For both measurements, the light source in the spectrophotometer passes through a 30 mm wide slit, producing two split optical beams: one serves as a reference beam, and the other is the signal beam hitting the sample with a 90° incidence angle. As in total transmittance setup, the PDMS film is put at the entrance of the chamber and the signal beam passes through the sample. All the light transmitted through the PDMS hits and scattered by standard white board (Labsphere SRS-90-010) and collected by photodetector. The normal transition of the PDMS is calculated after normalizing the intensity to the baseline signal.

Friction tests of modified elastomer surfaces

Static sliding friction tests were carried out to determine the coefficient of friction (COF) for virgin PDMS and HEMA_20. The sample is fixed on a stage with a deadweight of 20 g placed on the surface. Next, the stage is gradually tilted to increase the inclination angle, and the critical

angle (θ) at which the weight starts to slide is recorded (**Figure S4**). The static friction coefficient of the sample is determined from $\tan\theta$. The video of the experiment can be found online.

Dynamic sliding friction tests were performed in a ball-on-disc configuration. The tests were performed at three different automatically controlled normal loads at 1 N, 5 N, and 10 N. A linear reciprocating test with 10 mm s^{-1} speed and 5 mm stroke length were performed using a UMT-2 (Bruker, USA). All the tests were performed for 100 cycles. A 6.3 mm diameter chrome-steel ball was used as the counter surface. The counter surface was cleaned in acetone for 5 minutes, followed by isopropanol for 5 minutes before drying in nitrogen gas.

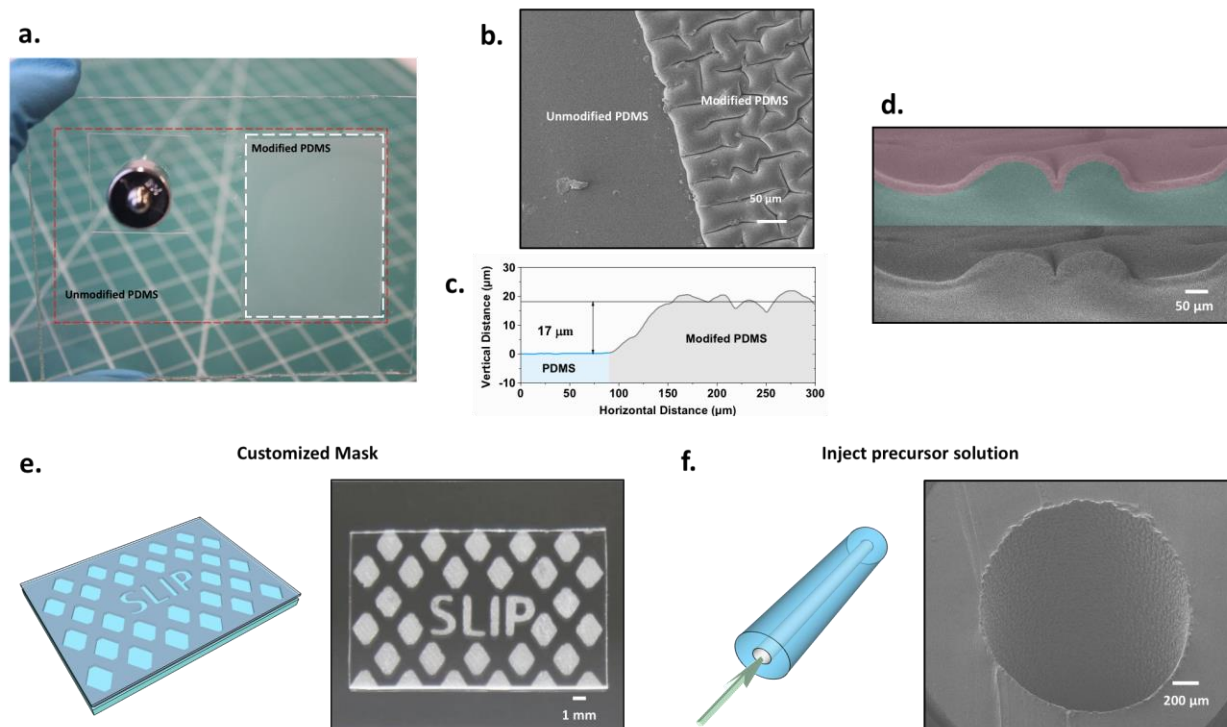


Figure 2. (a) Photograph showing entire PDMS (red square) with one region (white square) that has HEMA/PDMS hybrid skin layer grown. (b) Scanning electron microscope (SEM) image showing the boundary between unmodified and modified PDMS shown in (a). (c) Surface profile across the boundary from stylus measurement. (d) SEM image (bottom) showing the cross-section of the modified PDMS, and false-colored image (top) based on fractography, i.e., smoothness of the fractured surface. (e) Patterned skin layer (white regions) on PDMS using a custom mask of a “SLIP” acronym. (f) The skin layer is grown within the lumen of a PDMS microchannel. The surfaces in (d) and (e) were modified with 20 % HEMA precursor solution.

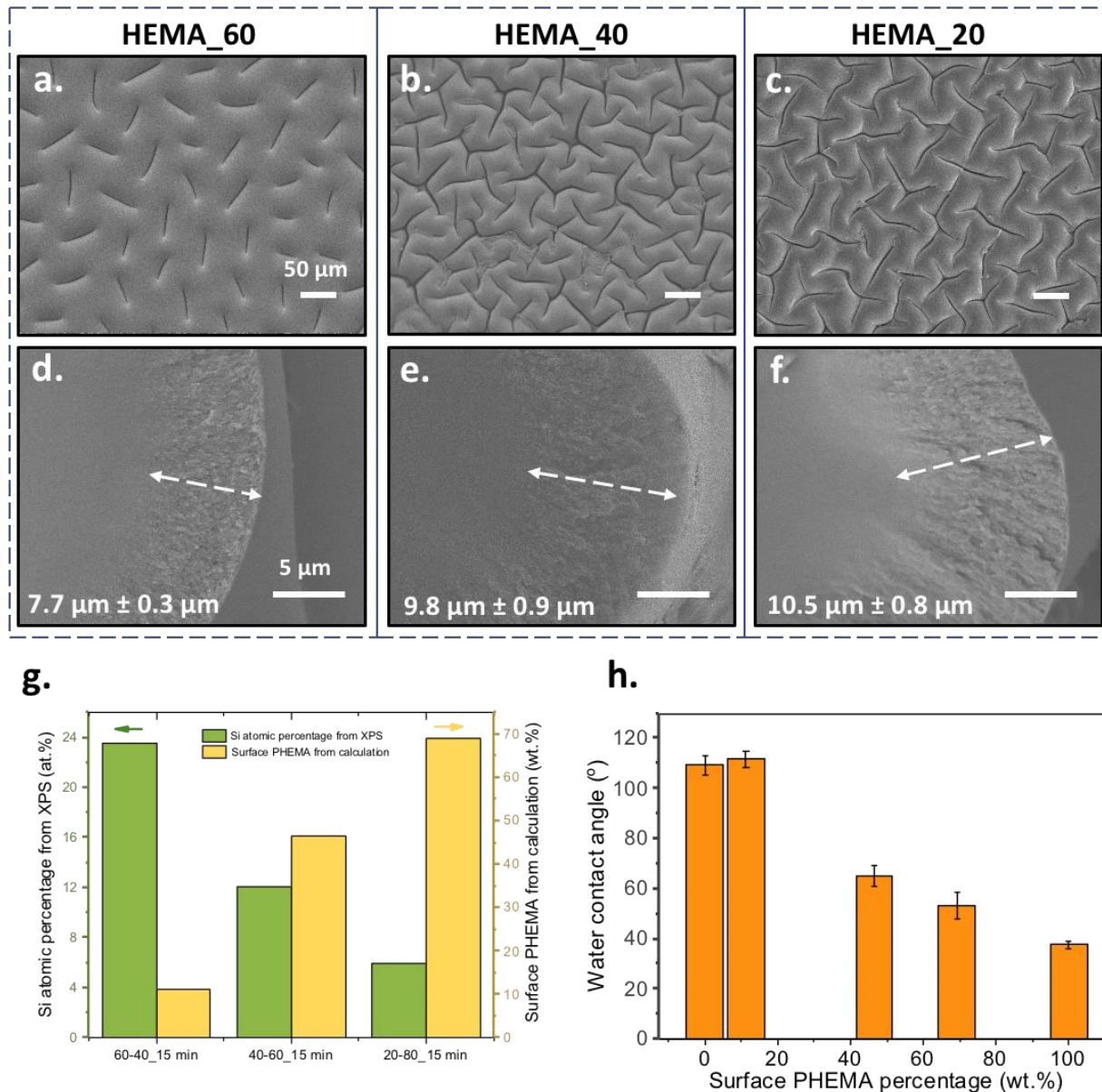


Figure 3. (a - c) SEM images of PDMS surfaces, modified using SLIP process with varying HEMA concentrations as labelled. (d - f) are the corresponding cross-sections of the samples shown in (a - c). The scale bars represent 50 μm in (a - c), and 5 μm in (d - f). (g) The atomic percentage of Si from X-ray photoelectron spectroscopy (XPS) measurements, and correspondingly the estimated PHEMA mass fraction, for skin layers grown using different HEMA precursor solutions. (h) Water contact angles of the skin layer as a function of PHEMA mass fraction determined in (g).

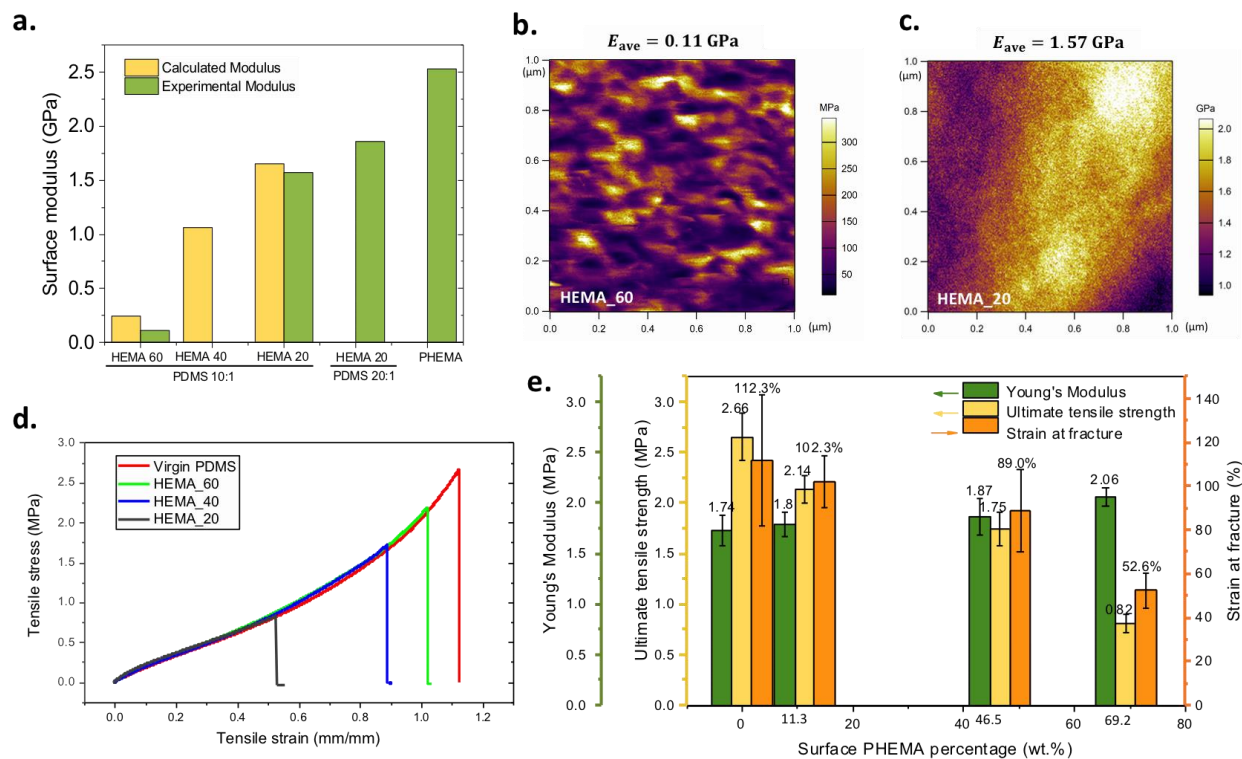


Figure 4. (a) Modulus of the skin layers calculated (yellow bars) according to PHEMA concentration from XPS measurements, as well as averaged from AFM (green bars) fast force mapping. (b) and (c) show the modulus map of skin layers from high-resolution AFM fast force mapping for HEMA_60 and HEMA_20. (d) Stress-strain curves from uniaxial tensile tests of PDMS with different skin layers, with corresponding Young's modulus, ultimate strength and strain-at-fracture summarized in (e).

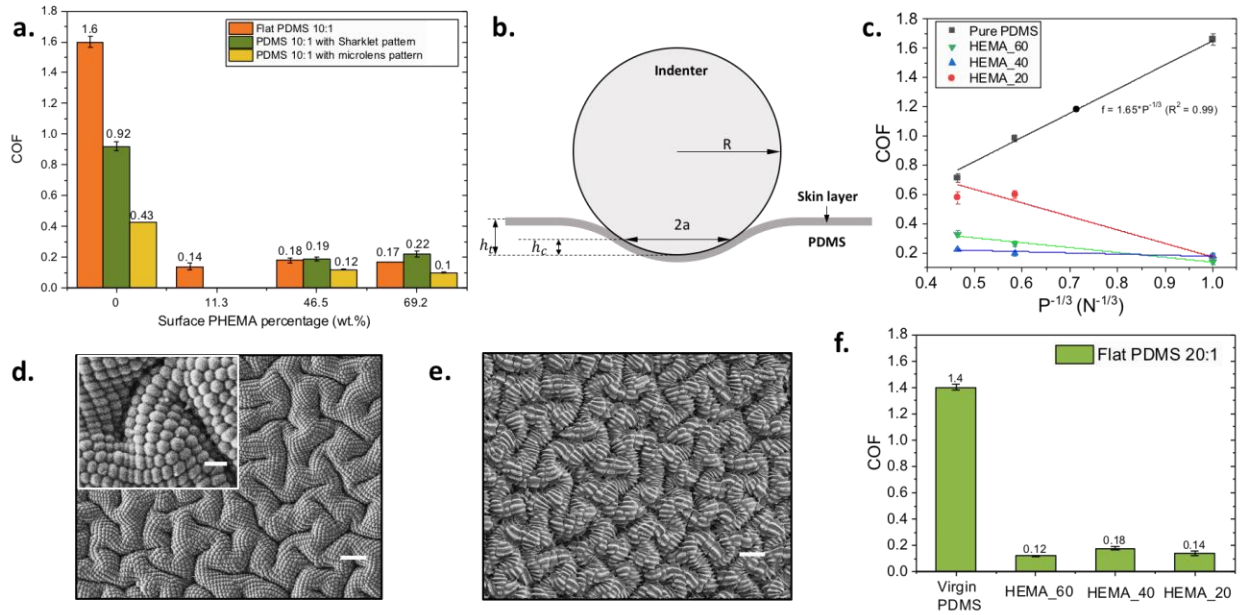


Figure 5. (a) Coefficient of friction (COF), under normal force $P = 1$ N as a function of surface PHEMA percentage for all PDMS 10:1 samples. (b) Illustration of detector tip with radius R contacting a compliant flat elastomer surface results in an indentation depth h_t , a contact depth h_c and a contact radius a . (c) COF as a function of $P^{-1/3}$. The lines represent linear fit of the experimental data. SEM images of the skin layers grown on PDMS prepatterned with (d) microlens array and (e) sharklet pattern. The scale bars represent $50 \mu\text{m}$. Inset of (d) shows the higher resolution SEM of a microlens patterned PDMS with a corresponding scale bar of $10 \mu\text{m}$. (f) COF (under 1 N normal force loading) for PDMS 20:1 prepared using varying HEMA precursor solutions. The surfaces in (d) and (e) were modified with 20 % HEMA precursor solution.

ASSOCIATED CONTENT

Supporting Information.

The Supporting Information available free of charge.

Section 1 - 14 contain PDMS surface after HEMA bulk polymerization; Monomer transfer in the SLIP process; Patterned PDMS samples; Examined samples; Surfaces of modified PDMS; Summary of surface topography; ATR-FTIR data; XPS data; Modulus of PDMS substrate; Surface modulus measurement; Dynamic sliding friction data; FEM simulation; Kinetic COF and normal load. (PDF)

Static sliding friction tests (MP4)

AUTHOR INFORMATION

Corresponding Author

* Yifu Ding, yifu.ding@colorado.edu

Author Contributions

M.W. conceived and designed the project. M.W. carried out the experiments and the characterizations unless stated otherwise below and wrote the manuscript. S.G. carried out the dynamic sliding friction tests. C.S. carried out the XPS experiment. A.B. carried out the surface modulus characterization. S.H. carried out the ATR-FTIR experiment. J.M. carried out the mechanical tests. R.L. devised the FEM analysis and theoretical calculation of elastomer surface under loading. C.B., J.M., M.Z. and Y.D. contributed to the experimental planning, theoretical guidance and manuscript preparation. All authors reviewed and approved the manuscript.

Funding Sources

This research is supported from innovative seed grant (ISG) from University of Colorado Boulder (CU-B), the National Science Foundation (NSF) Industry/University Cooperative Research Center for Membrane Science, Engineering and Technology (MAST) with Award IIP 1624602.

Notes

The authors declare that they have no competing interests.

Publication of the National Institute of Standards and Technology (NIST), an agency of the US government, not subject to copyright. Certain commercial equipment, instruments, or materials are identified in this paper to specify the experimental procedure adequately. Such identification does not imply recommendation or endorsement by NIST, nor does it imply that the materials or equipment identified are necessarily the best available for the purpose.

ACKNOWLEDGEMENT

M. W. and Y. D. acknowledge the funding supports from innovative seed grant (ISG) from University of Colorado Boulder (CU-B), the National Science Foundation (NSF) Industry/University Cooperative Research Center for Membrane Science, Engineering and Technology (MAST). J. M. acknowledges support from the NSF graduate research fellowship program (GRFP).

REFERENCES

1. Holmberg, K.; Erdemir, A. Influence of Tribology on Global Energy Consumption, Costs and Emissions. *Friction* **2017**, *5*, 263-284. DOI: 10.1007/s40544-017-0183-5.
2. Wu, Y. Y.; Tsui, W. C.; Liu, T. C. Experimental Analysis of Tribological Properties of Lubricating Oils with Nanoparticle Additives. *Wear* **2007**, *262*, 819-825. DOI: 10.1016/j.wear.2006.08.021.
3. Bollmann, W.; Spreadborough, J. Action of Graphite as a Lubricant. *Nature* **1960**, *186*, 29-30. DOI: 10.1038/186029a0.
4. Berman, D.; Erdemir, A.; Sumant, A. V. Graphene: A New Emerging Lubricant. *Mater. Today* **2014**, *17*, 31-42. DOI: 10.1016/j.mattod.2013.12.003.
5. Chawla, K.; Lee, S.; Lee, B. P.; Dalsin, J. L.; Messersmith, P. B.; Spencer, N. D. A Novel Low-Friction Surface for Biomedical Applications: Modification of Poly(dimethylsiloxane) (PDMS) with Polyethylene Glycol (PEG)-DOPA-lysine. *J. Biomed. Mater. Res. A* **2009**, *90*, 742-749. DOI: 10.1002/jbm.a.32141.
6. Martinez, R. V.; Branch, J. L.; Fish, C. R.; Jin, L.; Shepherd, R. F.; Nunes, R. M. D.; Suo, Z.; Whitesides, G. M. Robotic Tentacles with Three-dimensional Mobility Based on Flexible Elastomers. *Adv. Mater.* **2013**, *25*, 205-212. DOI: 10.1002/adma.201203002.
7. Shian, S.; Bertoldi, K.; Clarke, D. R. Dielectric Elastomer Based "Grippers" for Soft Robotics. *Adv. Mater.* **2015**, *27*, 6814-6819. DOI: 10.1002/adma.201503078.
8. Muth, J. T.; Vogt, D. M.; Truby, R. L.; Menguc, Y.; Kolesky, D. B.; Wood, R. J.; Lewis, J. A. Embedded 3D Printing of Strain Sensors within Highly Stretchable Elastomers. *Adv. Mater.* **2014**, *26*, 6307-6312. DOI: 10.1002/adma.201400334.
9. Trung, T. Q.; Lee, N. E. Flexible and Stretchable Physical Sensor Integrated Platforms for Wearable Human-Activity Monitoring and Personal Healthcare. *Adv. Mater.* **2016**, *28*, 4338-4372. DOI: 10.1002/adma.201504244.
10. Persson, B. N. J. On the Theory of Rubber Friction. *Surf. Sci.* **1998**, *401*, 445-454. DOI: 10.1016/S0039-6028(98)00051-X.
11. Barthlott, W.; Neinhuis, C. Purity of the Sacred Lotus, or Escape from Contamination in Biological Surfaces. *Planta* **1997**, *202*, 1-8. DOI: 10.1007/s004250050096.
12. Feng, L.; Li, S.; Li, Y.; Li, H.; Zhang, L.; Zhai, J.; Song, Y.; Liu, B.; Jiang, L.; Zhu, D. Super-Hydrophobic Surfaces: from Natural to Artificial. *Adv. Mater.* **2002**, *14*, 1857-1860. DOI: 10.1002/adma.200290020.

13. Autumn, K.; Liang, Y.; Hsieh, S.; Zesch, W.; Chan, W. P.; Kenny, T. W.; Fearing, R.; Full, R. J. Adhesive Force of a Single Gecko Foot-Hair. *Nature* **2000**, 405, 681-685. DOI: 10.1038/35015073.
14. Lee, H.; Dellatore, S. M.; Miller, W. M.; Messersmith, P. B. Mussel-Inspired Surface Chemistry for Multifunctional Coatings. *Science* **2007**, 318, 426-430. DOI: 10.1126/science.1147241.
15. Gans, C.; Baic, D. Regional Specialization of Reptilian Scale Surfaces - Relation of Texture and Biological Role. *Science* **1977**, 195, 1348-1350. DOI: 10.1126/science.195.4284.1348.
16. Carman, M. L.; Estes, T. G.; Feinberg, A. W.; Schumacher, J. F.; Wilkerson, W.; Wilson, L. H.; Callow, M. E.; Callow, J. A.; Brennan, A. B. Engineered Antifouling Microtopographies - Correlating Wettability with Cell Attachment. *Biofouling* **2006**, 22, 11-21. DOI: 10.1080/08927010500484854.
17. Wong, T. S.; Kang, S.; Tang, S.; Smythe, E. J.; Hatton, B. D.; Grinthal, A.; Aizenberg, J. Bioinspired Self-Repairing Slippery Surfaces with Pressure-Stable Omniphobicity. *Nature* **2011**, 477, 443-447. DOI: 10.1038/nature10447.
18. Bixler, G. D.; Bhushan, B. Fluid Drag Reduction with Shark-Skin Riblet Inspired Microstructured Surfaces. *Adv. Funct. Mater.* **2013**, 23, 4507-4528. DOI: 10.1002/adfm.201203683.
19. Klein, M. G.; Deuschle, J. K.; Gorb, S. N. Material Properties of the Skin of the Kenyan Sand Boa *Gongylophis Colubrinus* (Squamata, Boidae). *J. Comp. Physiol. A* **2010**, 196, 659-668. DOI: 10.1007/s00359-010-0556-y.
20. Dubansky, B. H. Close, M. A Review of Alligator and Snake Skin Morphology and Histotechnical Preparations. *J. Histotechnol.* **2019**, 42, 31-51. DOI: 10.1080/01478885.2018.1517856.
21. Jensen, J. B. Amphibians and Reptiles of Georgia, Athens: Univ. of Georgia Press, Georgia, US, 2008; p. 380.
22. Klein, M. G.; Gorb, S. N. Epidermis Architecture and Material Properties of the Skin of Four Snake Species. *J. R. Soc. Interface.* **2012**, 9, 3140-3155. DOI: 10.1098/rsif.2012.0479.
23. Jayne, B. C. Mechanical Behaviour of Snake Skin. *J. Zool.* **1988**, 214, 125-140. DOI: 10.1111/j.1469-7998.1988.tb04991.x.
24. Spinner, M.; Kovalev, A.; Gorb, S.; Westhoff, G. Snake Velvet Black: Hierarchical Micro- and Nanostructure Enhances Dark Colouration in *Bitis Rhinoceros*. *Sci. Rep.* **2013**, 3, 1846. DOI: 10.1038/srep01846.
25. Hu, D. L.; Nirody, J.; Scott, T.; Shelley, M. J. The Mechanics of Slithering Locomotion. *PNAS* **2009**, 106, 10081-10085. DOI: 10.1073/pnas.0812533106.

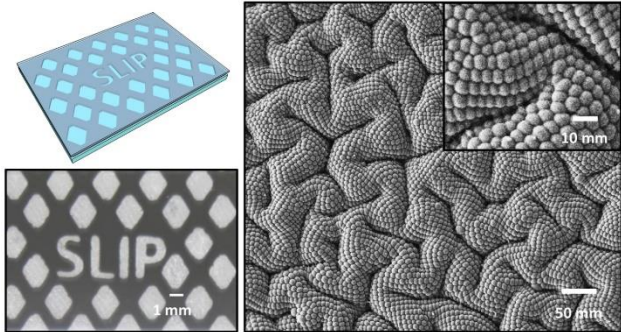
26. Berthe, R. A.; Westhoff, G.; Bleckmann, H.; Gorb, S. N. Surface Structure and Frictional Properties of the Skin of the Amazon Tree Boa *Corallus Hortulanus* (Squamata, Boidae). *J. Comp. Physiol. A* **2009**, 195, 311-318. DOI: 10.1007/s00359-008-0408-1.
27. Marvi, H.; Hu, D. L. Friction Enhancement in Concertina Locomotion of Snakes. *J. R. Soc. Interface* **2012**, 9, 3067-3080. DOI: 10.1098/rsif.2012.0132.
28. Rafsanjani, A.; Zhang, Y.; Liu, B.; Rubinstein, S. M.; Bertoldi, K. Kirigami Skins Make a Simple Soft Actuator Crawl. *Sci. Robot.* **2018**, 3, 7555. DOI: 10.1126/scirobotics.aar7555.
29. Ouyang, M.; Yuan, C.; Muisener, R. J.; Boulares, A.; Koberstein, J. T. Conversion of Some Siloxane Polymers to Silicon Oxide by UV/Ozone Photochemical Processes. *Chem. Mat.* **2000**, 12, 1591-1596. DOI: 10.1021/cm990770d.
30. Khorasani, M. T.; Mirzadeh, H.; Sammes, P. G. Laser Surface Modification of Polymers to Improve Biocompatibility: HEMA Grafted PDMS, in Vitro Assay - III. *Radiat. Phys. Chem.* **1999**, 55, 685-689. DOI: 10.1016/S0969-806X(99)00212-1.
31. Bodas, D.; Khan-Malek, C. Hydrophilization and Hydrophobic Recovery of PDMS by Oxygen Plasma and Chemical Treatment - An SEM Investigation. *Sens. Actuator B Chem.* **2007**, 123, 368-373. DOI: 10.1016/j.snb.2006.08.037.
32. George, S. M. Atomic Layer Deposition: An Overview. *Chem. Rev.* **2010**, 110, 111-131. DOI: 10.1021/cr900056b.
33. Alf, M. E.; Asatekin, A.; Barr, M. C.; Baxamusa, S. H.; Chelawat, H.; Ozaydin-Ince, G.; Petruczuk, C. D.; Sreenivasan, R.; Tenhaeff, W. E.; Trujillo, N. J.; Vaddiraju, S.; Xu, J.; Gleason, K. K. Chemical Vapor Deposition of Conformal, Functional, and Responsive Polymer Films. *Adv. Mater.* **2010**, 22, 1993-2027. DOI: 10.1002/adma.200902765.
34. Yu, Y.; Li, Z.; Wang, Y.; Gong, S.; Wang, X. Sequential Infiltration Synthesis of Doped Polymer Films with Tunable Electrical Properties for Efficient Triboelectric Nanogenerator Development. *Adv. Mater.* **2015**, 27, 4938-4944. DOI: 10.1002/adma.201502546.
35. Wang, Z.; Volinsky, A. A.; Gallant, N. D. Crosslinking Effect on Polydimethylsiloxane Elastic Modulus Measured by Custom-Built Compression Instrument. *J. Appl. Polym. Sci.* **2014**, 131, 41050. DOI: 10.1002/app.41050.
36. Wang, M.; Stafford, C. M.; Cox, L. M.; Blevins, A. K.; Aghajani, M.; Killgore, J. P.; Ding, Y. Controlled Growth of Polyamide Films atop Homogenous and Heterogeneous Hydrogels Using Gel-Liquid Interfacial Polymerization. *Macromol. Chem. Phys.* **2019**, 220, 1900100. DOI: 10.1002/macp.201900100.
37. Zhao, Z.; Xie, H.; An, S.; Jiang, Y. The Relationship between Oxygen Permeability and Phase Separation Morphology of the Multicomponent Silicone Hydrogels. *J. Phys. Chem. B* **2014**, 118, 14640-14647. DOI: 10.1021/jp507682k.

38. Lee, J. N.; Park, C.; Whitesides, G. M. Solvent Compatibility of Poly(dimethylsiloxane)-Based Microfluidic Devices. *Anal. Chem.* **2003**, *75*, 6544-6554. DOI: 10.1021/ac0346712.
39. Caykara, T.; Ozyurek, C.; Kantoglu, O.; Guven, O. Influence of Gel Composition on the Solubility Parameter of Poly (2-hydroxyethyl methacrylate-itaconic acid) Hydrogels. *J. Pol. Sci.* **2002**, *40*, 1995-2003. DOI: 10.1002/polb.10262.
40. Lee, M.; Cho, B.; Zin, W. Supramolecular Structures from Rod-Coil Block Copolymers. *Chem. Rev.* **2001**, *101*, 3869-3892. DOI: 10.1021/cr0001131.
41. Guvendiren, M.; Yang, S.; Burdick, J. A. Swelling-Induced Surface Patterns in Hydrogels with Gradient Crosslinking Density. *Adv. Funct. Mater.* **2009**, *19*, 3038-3045. DOI: 10.1002/adfm.200900622.
42. Guvendiren, M.; Burdick, J. A.; Yang, S. Solvent Induced Transition from Wrinkles to Creases in Thin Film Gels with Depth-Wise Crosslinking Gradients. *Soft Matter* **2010**, *6*, 5795-5801. DOI: 10.1039/c0sm00317d.
43. Kim, H. S.; Crosby, A. J. Solvent-Responsive Surface via Wrinkling Instability. *Adv. Mater.* **2011**, *23*, 4188-4192. DOI: 10.1002/adma.201101477.
44. Rahmawan, Y.; Chen, C. M.; Yang, S. Recent Advances in Wrinkle-Based Dry Adhesion. *Soft Matter*, **2014**, *10*, 5028-5039. DOI: 10.1039/C4SM00027G.
45. Lin, P. C.; Vajpayee, S.; Jagota, A.; Hui, C. Y.; Yang, S. Mechanically Tunable Dry Adhesive from Wrinkled Elastomers. *Soft Matter*, **2008**, *4*, 1830-1835. DOI: 10.1039/B802848F.
46. Tanaka, T.; Sun, S. T.; Hirokawa, Y.; Katayama, S.; Kucera, J.; Hirose, Y.; Amiya, T. Mechanical Instability of Gels at the Phase Transition. *Nature*, **1987**, *325*, 796-798. DOI: 10.1038/325796a0.
47. Hayward R. C.; Chmelka, B. F.; Kramer E. J. Template Cross-Linking Effects on Morphologies of Swellable Block Copolymer and Mesostructured Silica Thin Films *Macromolecules*, **2005**, *38*, 7768-7783. DOI: 10.1021/ma0477854.
48. Wang, Q.; Zhao, X. A Three-Dimensional Phase Diagram of Growth-Induced Surface Instabilities. *Sci. Rep.* **2015**, *5*, 8887. DOI: 10.1038/srep08887.
49. Bertrand T.; Peixinho J.; Mukhopadhyay S.; MacMinn C. W. Dynamics of Swelling and Drying in a Spherical Gel. *Phys. Rev. Appl.* **2016**, *6*, 064010. DOI: 10.1103/PhysRevApplied.6.064010.
50. Abdel-Aal, H. A. On Surface Structure and Friction Regulation in Reptilian Limbless Locomotion. *J. Mech. Behav. Biomed.* **2013**, *22*, 115-135. DOI: 10.1016/j.jmbbm.2012.09.014.

51. Cao, C.; Chan, H. F.; Zang, J.; Leong, K. W.; Zhao, X. Harnessing Localized Ridges for High-Aspect-Ratio Hierarchical Patterns with Dynamic Tunability and Multifunctionality. *Adv. Mater.* **2014**, 26, 1736-1770. DOI: 10.1002/adma.201304589.
52. Stafford, C.; Harrison, C.; Beers, K.; Karim, A.; Amis, E. J.; VanLandingham, M. R.; Kim, H.C.; Volksen, W.; Miller, R. D.; Simonyi, E. E. A Buckling-Based Metrology for Measuring the Elastic Moduli of Polymeric Thin Films. *Nat. Mater.* **2004**, 3, 545–550. DOI: 10.1038/nmat1175
53. Wilder, E. A.; Guo, S.; Lin-Gibson, S.; Fasolka, M. J.; Stafford, C. M. Measuring the Modulus of Soft Polymer Networks via a Buckling-Based Metrology. *Macromolecules* **2006**, 39, 4138-4143. DOI: 10.1021/ma060266b.
54. Wang, M.; Gorham, J. M.; Killgore, J. P.; Omidvar, M.; Lin, H.; DelRio, F.; Cox, L.; Zhang, Z.; Ding, Y. Formation of a Crack-Free, Hybrid Skin Layer with Tunable Surface Topography and Improved Gas Permeation Selectivity on Elastomers Using Gel-Liquid Infiltration Polymerization. *ACS Appl. Mater. Interfaces* **2017**, 9, 28100-28106. DOI: 10.1021/acsami.7b09274.
55. Jin, M.; Feng, X.; Xi, J.; Zhai, J.; Cho, K.; Feng, L.; Jiang, L. Super-Hydrophobic PDMS Surface with Ultra-Low Adhesive Force. *Macromol. Rapid Commun.* **2005**, 26, 1805-1809. DOI: 10.1002/marc.200500458.
56. Rodriguez-Emmenegger, C.; Avramenko, O. A.; Brynda, E.; Skvor, J.; Alles, A. B. Poly(HEMA) Brushes Emerging as a New Platform for Direct Detection of Food Pathogen in Milk Samples. *Biosens. Bioelectron.* **2011**, 26, 4545-4551. DOI: 10.1016/j.bios.2011.05.021.
57. Cassie, A. B. D.; Baxter, S. Wettability of Porous Surfaces. *Trans. Faraday Soc.* **1944**, 40, 546-550. DOI: 10.1039/TF9444000546.
58. Willemse, R. C.; Speijer, A.; Langeraar, A. E.; Posthuma de Boer, A. Tensile Moduli of Co-continuous Polymer Blends. *Polymer* **1999**, 40, 6645-6650. DOI: 10.1016/S0032-3861(98)00874-X.
59. Cox, L. M.; Blevins, A. K.; Drisko, J. A.; Qi, Y.; Ding, Y.; Fiedler-Higgins, C. I.; Long, R.; Bowman, C. N.; Killgore, J. P. Tunable Mechanical Anisotropy, Crack Guiding, and Toughness Enhancement in Two-Stage Reactive Polymer Networks. *Adv. Eng. Mater.* **2019**, 21, 1900578. DOI: 10.1002/adem.201900578.
60. Ghosh, S. K.; Miller, C.; Choudhury, D.; Goss, J. A.; Zou, M. The Effects of PTFE Thickness on the Tribological Behavior of Thick PDA/PTFE Coatings. *Tribol. Trans.* **2020**, 63, 575-584. DOI: 10.1080/10402004.2020.1728001.
61. He, B.; Chen, W.; Wang, Q. J. Surface Texture Effect on Friction of a Microtextured Poly(dimethylsiloxane) (PDMS). *Tribol. Lett.* **2008**, 31, 187-197. DOI: 10.1007/s11249-008-9351-0.

62. Kendall, K. The Adhesion and Surface Energy of Elastic Solids. *J. Phys. D Appl. Phys.* **1971**, 4, 1186-1195. DOI: 10.1088/0022-3727/4/8/320.
63. Etsion, I. State of the Art in Laser Surface Texturing. *J. Tribol-T. ASME* **2005**, 127, 248-253. DOI: 10.1115/1.1828070.
64. Maniglio, D.; Ding, Y.; Wang, L.; Migliaresi, C. One-Step Process to Create Porous Structures in Cross-Linked Polymer Films via Breath-Figure Formations during in Situ Cross-Linking Reactions. *Polymer* **2011**, 52, 5102-5106. DOI: 10.1016/j.polymer.2011.08.054.
65. Fan, S.; Aghajani, M.; Wang, M.; Martinez, J.; Ding, Y. Patterning Flat-Sheet Poly (vinylidene fluoride) Membrane Using Templated Thermally Induced Phase Separation. *J. Membr. Sci.* **2020**, 626, 118627. DOI: 10.1016/j.memsci.2020.118627.
66. Galliano, A.; Bistac, S.; Schultz, J. Adhesion and Friction of PDMS Networks: Molecular Weight Effects. *J. Colloid Interface Sci.* **2003**, 265, 372-379. DOI: 10.1016/s0021-9797(03)00458-2.

TOC graphic



Supporting Information

Snakeskin-inspired Elastomers with Extremely Low Coefficient of Friction under Dry Conditions

Mengyuan Wang,^{1,2} Sujan K. Ghosh,³ Christopher M. Stafford,⁴ Adrienne K. Blevins,^{1,2} Sijia Huang,⁵ Jaylene Martinez,² Rong Long,² Christopher N. Bowman,^{1,5} Jason P. Killgore,⁶ Min Zou³ and Yifu Ding^{1,2,}*

¹Materials Science and Engineering Program, University of Colorado, Boulder, CO, 80303, the United States

²Department of Mechanical Engineering, University of Colorado, Boulder, CO, 80309, the United States

³Department of Mechanical Engineering, University of Arkansas, Fayetteville, AR 72701, the United States

⁴Materials Science and Engineering Division, National Institute of Standards and Technology, Gaithersburg, MD, 20899, the United States

⁵Department of Chemical and Biochemical Engineering, University of Colorado, Boulder, CO, 80309, the United States

⁶Applied Chemicals and Materials Division, National Institute of Standards and Technology, Boulder, CO 80305, the United States

*Corresponding author. Email: yifu.ding@colorado.edu

This PDF file includes:

Section S1 to S14
Figure S1 to S10
Table S1 to S6
References
Movie S1

S1. Polydimethylsiloxane (PDMS) surface after 2-hydroxyethyl methacrylate (HEMA) bulk photopolymerization atop.

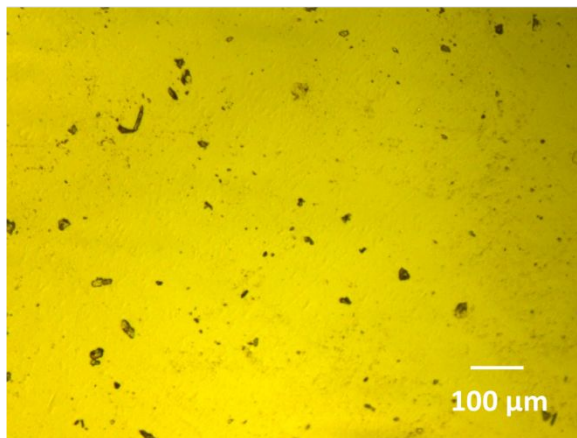


Figure S1. Optical microscope image of PDMS surface after HEMA bulk photopolymerization (i.e., in the absence of water).

S2. Illustration of monomers transfer in the Solid-Liquid Interfacial Polymerization (SLIP) process

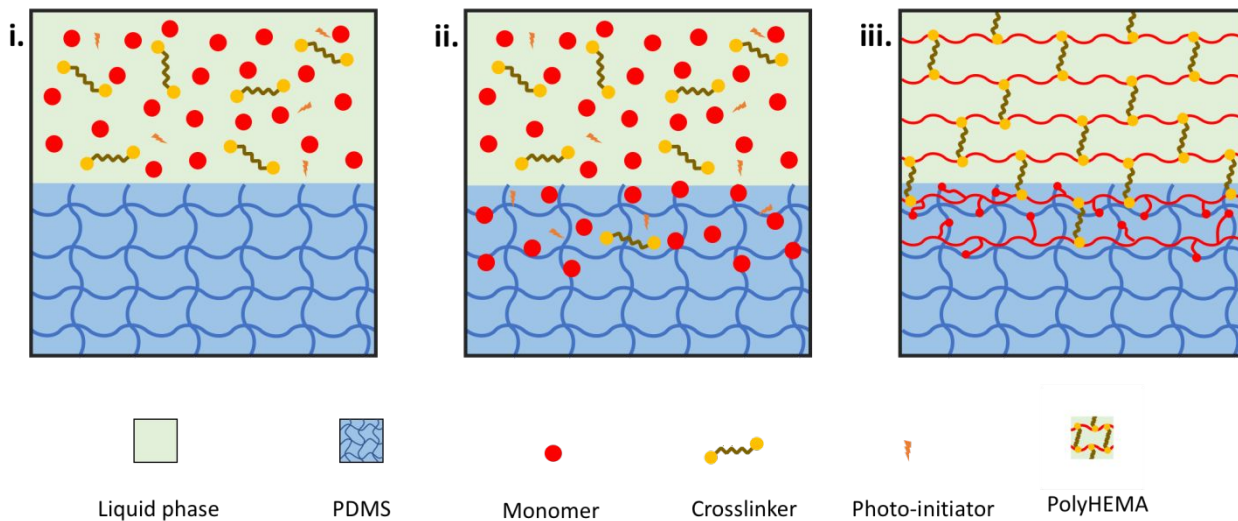


Figure S2. Illustration of monomer/polymer infiltration and polymerization in PDMS surface network.

S3. Patterned PDMS samples

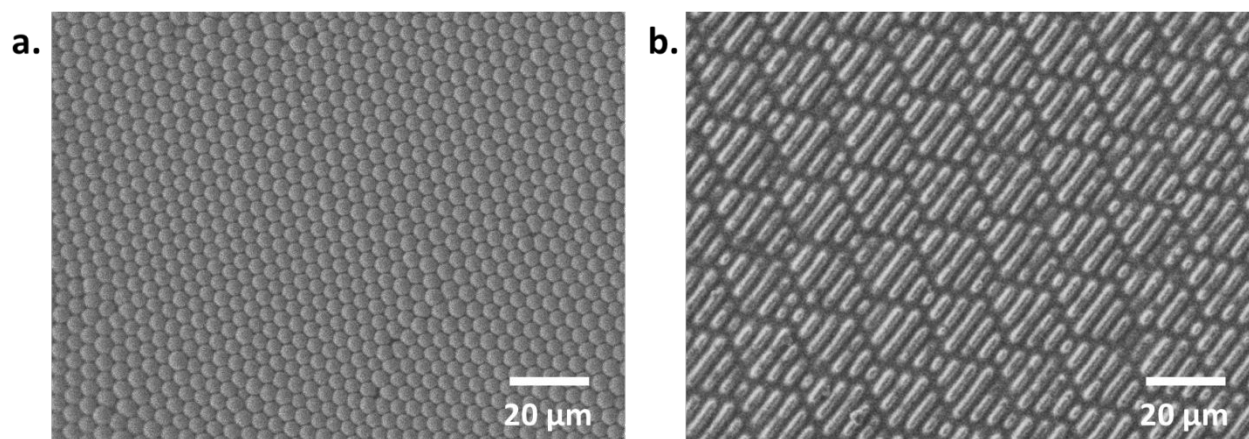


Figure S3. SEM images of the PDMS with (A) microlens array, and (B) Sharklet patterns.

S4. Examined samples

Table S1. Summary of the SLIP process conditions used in this study

PDMS	Pre-pattern	Reaction time (min)	Monomer (% by mass) - water (% by mass)
10:1	None	15	60-40
10:1	None	15	40-60
10:1	None	15	20-80
10:1	None	15	20-80
20:1	None	15	20-80
5:1	None	15	20-80
10:1	None	30	20-80
10:1	Sharklet AF TM	15	20-80
10:1	Microlens array	15	20-80

S5. Static sliding friction tests

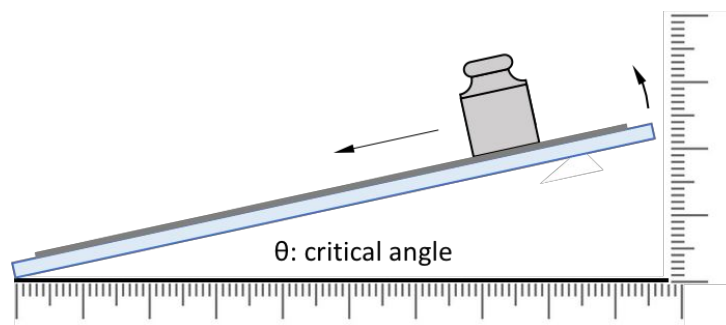


Figure S4. Schematics of the sliding friction behavior test.

S6. SEM images of surface morphology of skin layers of modified PDMS

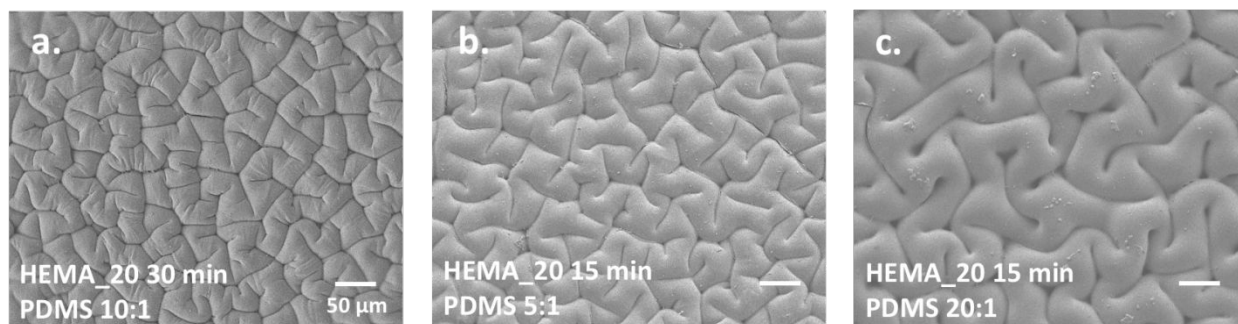


Figure S5. SEM image of surface morphology of PDMS modified with HEMA₂₀ solution (A) PDMS 10:1 for 30 min, (B) PDMS 5:1 for 15 min, and (C) PDMS 20:1 for 15 min.

S7. Feature type and corresponding size of the topography on the skin layers

Table S2. Summary of modified PDMS surface morphology and corresponding feature size

Reaction time	PDMS substrate	HEMA/water ratio	Morphology	lateral size (μm)	Vertical size (μm)	Aspect ratio	
15 min	5:1	20/80	Cuneiform-like creases	28.9 ± 6.4	5.6 ± 1.8	0.19	
	10:1	20/80	Cuneiform-like creases	28.9 ± 8.1	6.3 ± 1.3	0.21	
		40/60	Cuneiform-like creases	27.2 ± 4.4	4.9 ± 1.6	0.18	
		60/40	Isolated linear creases	Distance between adjacent parallels	56.0 ± 9.7	5.9 ± 1.3	0.10
				Length of the line	38.0 ± 8.8		
20:1	20/80	Deep creases	41.1 ± 10.5	17.0 ± 4.9	0.41		
30 min	10:1	20/80	Creases with hierarchical structure	Large crease	31.7 ± 5.0	6.7 ± 1.7	0.21
				Small crease	7.0 ± 1.2		

S8. ATR-FTIR analysis

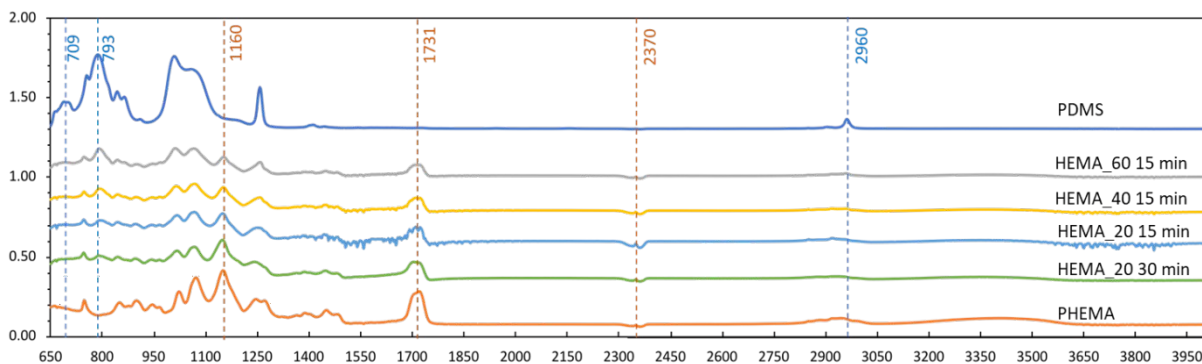


Figure S6. ATR-FTIR spectra of PDMS, PHEMA hydrogel and modified PDMS surfaces. The characteristic absorption bands of PDMS and PHEMA corresponding groups are indicated by blue and orange dash lines, respectively.

Table S3. IR absorbance band (cm^{-1}) of PDMS, PHEMA and modified PDMS films

Assignments	PHEMA ^{a)}	PDMS ^{b)}	Modified PDMS
Si-C vibration	-	709	696
Si-O-Si stretching	-	793	799
methyl groups	-	2970	2969
C-O stretching	1160	-	1158
C=O stretching	1731	-	1727
	2360	-	2358
hydroxyl group	3100 - 3700	-	3100 - 3700

Reference of IR spectra for characteristic vibrations in a) PHEMA; ^{1, 2, 3} b) PDMS. ^{2, 4}

S9. XPS analysis

Table S4. Surface chemical composition of modified PDMS by XPS measurement.

Sample	C (%)	O (%)	Si (%)	C from PDMS (%)	PDMS (wt. %)	PDMS (v. %)
PDMS ^{a)}	47.1	25.1	27.7	-	-	
60-40-15 min	66.3	27.7	6.0	10.2	88.7	90.3
40-60-15 min	61.1	26.8	12.1	20.6	53.6	57.9
20-80-15 min	51.6	24.8	23.6	40.1	30.8	34.6

a) Data from reference 5.

The weight percentage of PDMS (w_P) in the skin layer is estimated based on the atomic percentage of Si from XPS given the stoichiometry of PDMS. The volume fraction of PDMS (V_P) is estimated using density of PDMS ($\rho_P = 0.97 \text{ g/cm}^3$) and PHEMA ($\rho_H = 1.15 \text{ g/cm}^3$),

$$V_P = \frac{w_P \cdot \rho_H}{w_P \cdot \rho_H + w_H \cdot \rho_P} \quad (\text{S1})$$

S10. Modulus of hybrid skin layer and PDMS substrate

Table S5. Summaries of modulus of hybrid skin layer and PDMS substrate

PDMS	Reaction conditions	Substrate modulus (MPa)	Hybrid skin layer modulus (GPa)
10:1	60-40-15 min	1.8 ± 0.2	0.24
	40-60-15 min	1.8 ± 0.2	1.06
	20-80-15 min	1.8 ± 0.2	1.65
5:1	20-80-15 min	1.5(tensile) 2.7 (buckling) ^{a)}	N/A
20:1		0.65	N/A

a) Data from reference 6.

S11. Surface modulus measurement by AFM fast force mapping

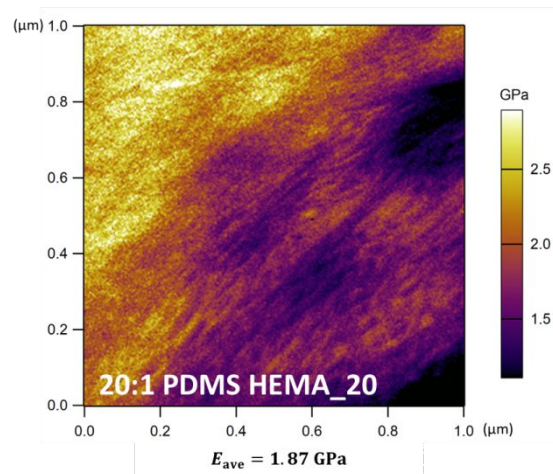


Figure S7. Modulus map of skin layers from high-resolution AFM fast force mapping for HEMA_20 by using PDMS 20:1.

S12. Dynamic sliding friction behavior of PDMS samples

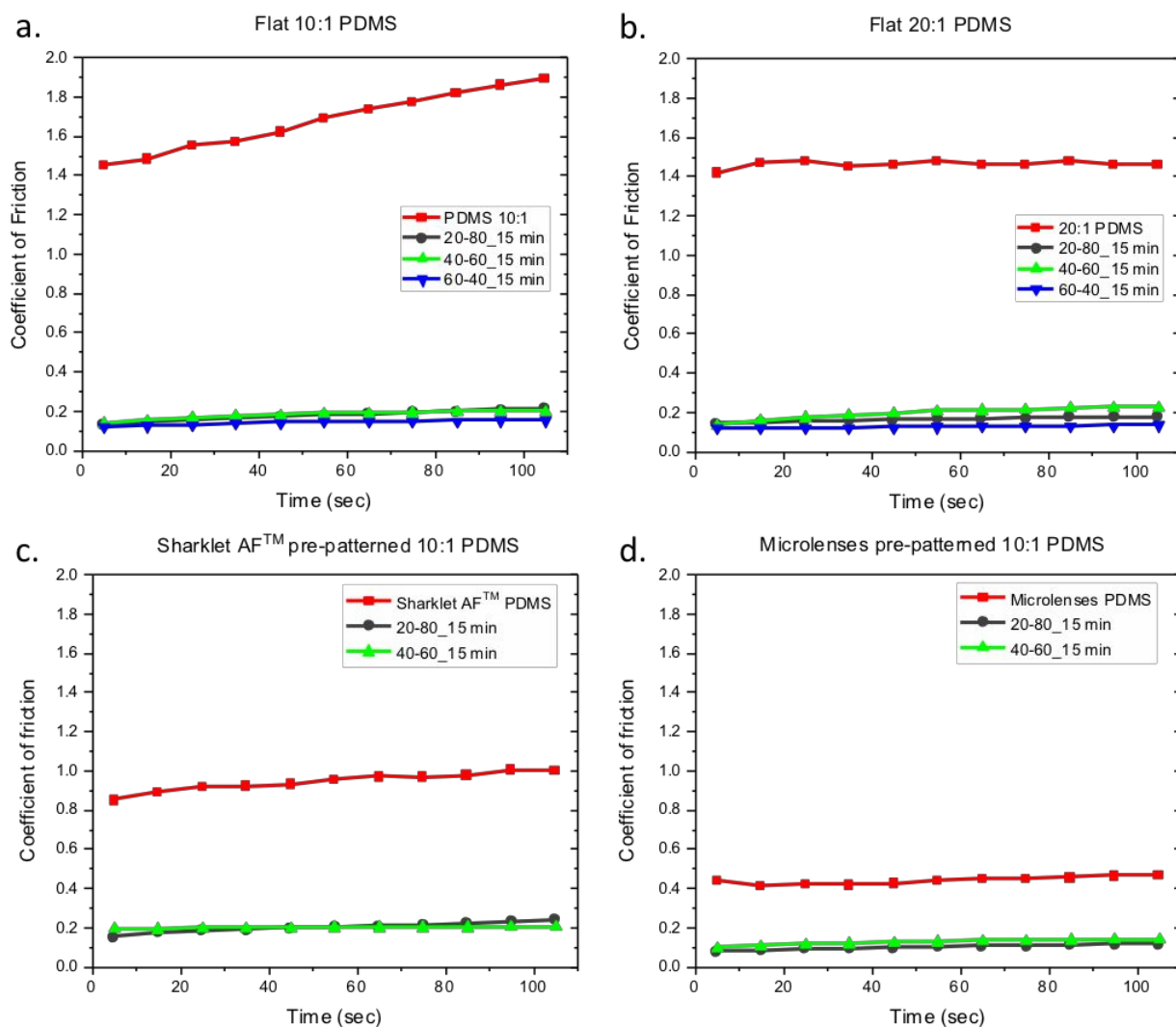


Figure S8. Summary of the multiple cycles of COF measurements for PDMS samples under 1 N load. (A) 10:1 PDMS samples, (B) 20:1 PDMS samples, (C) Sharklet AFTM pre-patterned PDMS samples and (D) Microlens pre-patterned PDMS samples.

S13. Finite Element Modeling (FEM) simulation of contact area and contact depth

We estimated the contact areas between the spherical Chrome steel indenter and the PDMS using FEM simulation. For all modeling cases, the steel indenter (radius $R = 3.15 \text{ mm}$) is treated as rigid (i.e. no deformation) with an elastic modulus and Poisson's ratio of 265 GPa and 0.2, respectively. The thickness of all the PDMS samples is 1 mm. For unmodified PDMS, the elastic modulus and Poisson's ratio are 1.74 MPa and 0.5, respectively. The SLIP-modified PDMS samples are treated as bi-layers with a smooth, homogenous skin layer atop the unmodified PDMS. The elastic moduli of the skin layers are 0.11 GPa (HEMA_60, AFM measurement), 1.07 GPa (HEMA_40, calculated value from mixing rule), and 1.57 GPa (HEMA_20, AFM measurement), respectively. The Poisson's ratios of the skin layers are estimated, using composite rule based on PHEMA/PDMS composition, as 0.48, 0.42 and 0.37, for HEMA_60, HEMA_40, and HEMA 20. Note that, the variation of Poisson's ratio, from 0.32 (glassy state PHEMA) to 0.5 (pure PDMS), has a negligible impact on the results obtained below. Lastly, the thickness of the skin layer is 8 μm , 10 μm and 10 μm for HEMA_60, HEMA_40, and HEMA_20, respectively,

The real contact depth h_c , as illustrated in **Figure 5b** in the main text, can be calculated as:

$$h_c = R - \sqrt{R^2 - a^2} \quad (\text{S2})$$

Figure S9 show the stress profile of PDMS and HEMA_20 under 1N normal force loading.

Figure S10 summarizes the force-contact area relationship for the four samples obtained from the FEM simulation. Most importantly, the simulated contact area A (estimated as πa^2) and the real contact depth h_c under 1 N normal force loading are listed in **Table S6**.

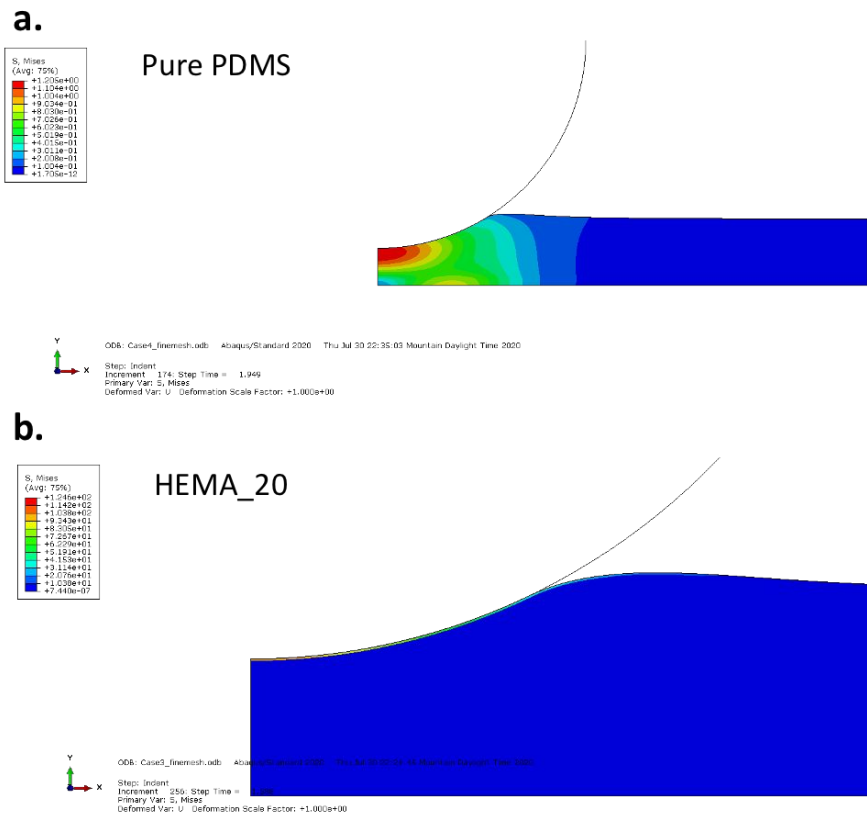


Figure S9. FEM simulation of normal indentation on: (A) the pure PDMS and (B) the modified PDMS HEMA_20.

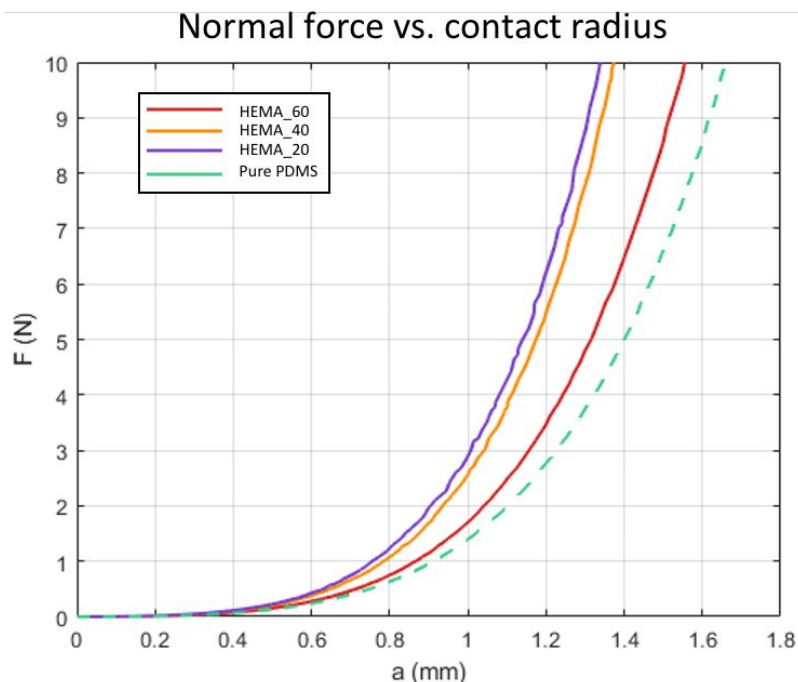


Figure S10. Relationship between normal force and contact radius obtained from FEM simulation.

Table S6. Estimated contact area under 1N load from FEM simulation

Samples	Contact area πa^2 (mm ²)	Real contact depth h_c (mm)
Pure PDMS ^{a)}	0.91	0.15
60-40_15 min	0.87	0.14
40-60_15 min	0.78	0.13
20-80_15 min	0.76	0.13

^{a)} The Young's Modulus of HEMA_40 PDMS surface was used from the calculated result by polymer blender model, otherwise applied Young's Modulus was from experiment data by AFM modulus mapping measurement.

Above analysis shows that the hybrid skin layer slightly reduces the contact deformation of the PDMS surface. The PDMS substrate is much thicker than the skin layer, so that the contact radius is still dominated by the soft PDMS under normal force range of 1 N to 10 N, as employed in this study.

S14. Relationships between kinetic COF and the normal load P

The kinetic friction coefficient under sliding, μ_D , is defined as,

$$\mu_D = \frac{f}{P} \quad (\text{S3})$$

where f and P are the tangential (friction) force and normal force experienced by the sliding sphere. The friction force f can be estimated by,

$$f = A\tau \quad (\text{S4})$$

where A is the contact area and τ is the frictional shear stress within the contact area. Substituting Equation S3 into Equation S4 results in the following expression for the kinetic friction coefficient,

$$\mu_D = \frac{A\tau}{P} = \frac{\tau}{\sigma} \quad (\text{S5})$$

where $\sigma = P/A$ is the average contact pressure. The frictional shear stress τ can be calculated using Persson's theory.⁷ Without engaging mathematical details of this theory, we note that τ is determined by matching the power of frictional dissipation and the rate of viscoelastic loss in the elastomer substrate. As a result, τ was found to depend on the sliding velocity, the viscoelastic complex modulus of the substrate, and the surface roughness, but independent of the normal load P or contact pressure σ (assuming small deformation). Next, we use Equation S5 to discuss the scaling relation between μ_D and P .

(1) For non-patterning PDMS surface

We model the unmodified PDMS as an infinite substrate with a smooth surface. According to Persson,⁷ the friction shear stress τ is constant under a given sliding velocity and is independent of the normal load P . On the other hand, the average normal pressure σ depends on both P and contact area A ,

$$\sigma = \frac{P}{A} \quad (\text{S6})$$

and the real contact area A ($A = \pi a^2$, a is the radius of real contact area) can be determined by the Hertz theory,⁸

$$a^3 = \frac{3R}{4E^*}P \quad (\text{S7})$$

The equivalent modulus, E^* , is estimated using:

$$\frac{1}{E^*} = \frac{1 - \nu_p^2}{E_p} + \frac{1 - \nu_t^2}{E_t} \quad (\text{S8})$$

where E is the elastic modulus and ν is the Poisson's ratio, the subscript “ P ” and “ i ” corresponds to PDMS and the indenter tip, correspondingly. Therefore, the average normal σ and P has the following relationship,

$$\sigma = \frac{P}{A} = \frac{P}{\pi a^2} = \frac{1}{\pi} \left(\frac{3R}{4E^*} \right)^{-2/3} P^{1/3} \propto P^{1/3} \quad (\text{S9})$$

Combining Equation S5 and S9, we find that

$$\mu_D = \frac{\tau}{\sigma} \propto P^{-1/3} \quad (\text{S10})$$

(2) For the modified PDMS surface with creased skin layers

The PHEMA/PDMS skin layer differ from the non-patterning PDMS in both the gradient stiffness and the surface roughness. The creasing structure makes the real contact area, denoted as A_R , smaller than the nominal contact area A as in the case of a non-patterning surface. As a result, the nominal contact area A in Equation S4 and S5 should replace by the real contract area, yielding

$$\mu_D = \frac{A_R \tau}{P} = \frac{A_R \tau}{A \sigma} = \frac{\tau A_R}{\sigma A} \quad (\text{S11})$$

where $\sigma = P/A$ is the average contact pressure based on the nominal contact area. The ratio A_R/A , ranging from 0 to 1, depends on the native surface roughness profile as well as the average contact pressure σ which acts to flatten the surface roughness. A good approximation of A_R/A can be obtained at small contact pressure σ as $A_R/A \sim \sigma^{-7}$, which leads to

$$\mu_D \sim \tau \quad (\text{S12})$$

Depending on the dependency of τ on P , the two following scenarios can occur:

- If we assume τ remains constant under a fixed sliding velocity, μ_D becomes a constant and independent of P , a behavior agrees with Coulomb friction.
- However, if τ increases with P , due to the flattening of the asperities/features, μ_D increases with P , which leads to the trend observed in **Figure 5c**.

S15. Normal transmission and total transmission of PDMS films

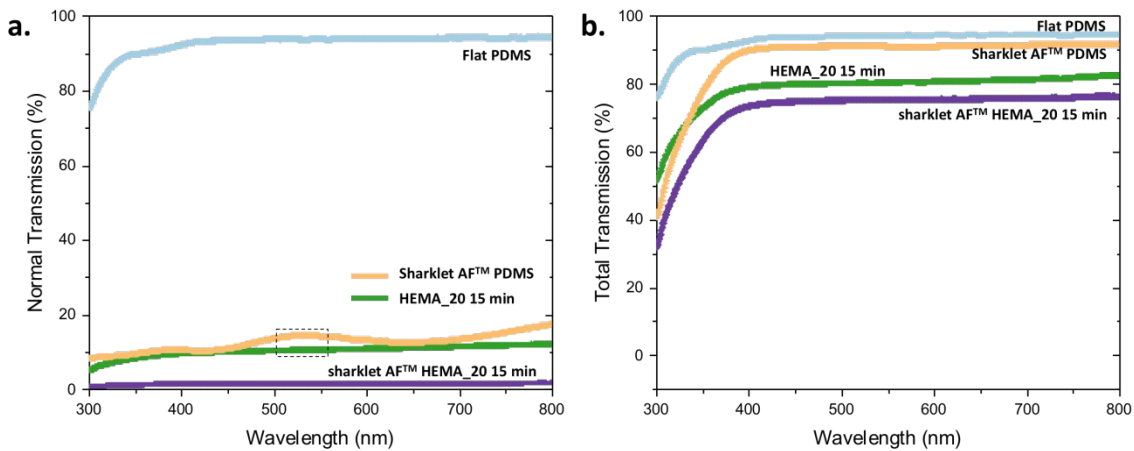


Figure S11. (a) Normal transmission and (b) total transmission of flat PDMS, Sharklet patterned PDMS and SLIP modified PDMS films (both flat and Sharklet-patterned).

References

1. Cao, B.; Yang, M.; Hu, G. Capillary Filling Dynamics of Polymer Melts in Nanopores: Experiments and Rheological Modelling. *RSC Adv.* **2016**, *6*, 7553-7559. DOI: 10.1039/C5RA24991K.
2. Ferreira, P.; Carvalho, A.; Correia, T. R.; Antunes, B. P.; Correia, I. J.; Alves, P. Functionalization of Polydimethylsiloxane Membranes to be Used in the Production of Voice Prostheses. *Sci. Technol. Adv. Mater.* **2013**, *14*, 055006. DOI: 10.1088/1468-6996/14/5/055006.
3. Khorasani, M. T.; Mirzadeh, H.; Sammes, P. G. Laser Surface Modification of Polymers to Improve Biocompatibility: HEMA Grafted PDMS, in Vitro Assay - III. *Radiat. Phys. Chem.* **1999**, *55*, 685-689. DOI: 10.1016/S0969-806X(99)00212-1.
4. Maji, D.; Lahiri, S. K.; Das, S. Study of Hydrophilicity and Stability of Chemically Modified PDMS Surface Using Piranha and KOH Solution. *Surf. Interface Anal.* **2012**, *44*, 62-69. DOI: 10.1002/sia.3770.
5. Schnyder, B.; Lippert, T.; Kotz, R.; Wokaun, A.; Graubner, V. M.; Nuyken, O. UV-Irradiation Induced Modification of PDMS Films Investigated by XPS and Spectroscopic Ellipsometry. *Surf. Sci.* **2003**, 532-535, 1067-1071. DOI: 10.1016/S0039-6028(03)00148-1.
6. Wilder, E. A.; Guo, S.; Lin-Gibson, S.; Fasolka, M. J.; Stafford, C. M. Measuring the Modulus of Soft Polymer Networks via a Buckling-Based Metrology. *Macromolecules* **2006**, *39*, 4138-4143. DOI: 10.1021/ma0615607.
7. Persson, B.N.J. Theory of Rubber Friction and Contact Mechanics. *J. Chem. Phys.* **2001**, *115*, 3840-3861. DOI: 10.1063/1.1388626.
8. Carrillo, F.; Gupta, S.; Balooch, M.; Marshall, S.; Marshall, G.; Pruitt, L.; Puttlitz, C. Nanoindentation of Polydimethylsiloxane Elastomers: Effect of Crosslinking, Work of Adhesion, and Fluid Environment on Elastic Modulus. *J. Mater. Res.* **2005**, *20*, 2820-2830. DOI: 10.1557/JMR.2005.0354.